RADIOASTRONOMY

THE STUDY OF EXTRAGALACTIC SOURCES 3C 446 AND 3C 345 WITH USING THE SINGULAR SPECTRUM AND WAVELET ANALYSIS

G.I.Donskykh [1], M.I.Ryabov [2], A.L.Sukharev [2], M.F.Aller [3]

[1] Department of Astronomy, I.I.Mechnikov Odessa National University, Ukraine
[2] Odessa observatory "URAN-4" of the Institute of Radio Astronomy NAS, Ukraine
[3] Radio observatory of Michigan University, Ann Arbor, USA

ABSTRACT. We investigated the data of monitoring of flux density of extragalactic sources 3C446 and 3C345, which was held on 26-meter radio telescope of University of Michigan at frequencies 14.5, 8 and 4.8 GHz. The data of observations were investigated using singular spectrum analysis and wavelet-analysis. According to the results of wavelet analysis for each year of observations, graphics of "spectra periods" were built to determine the contribution of individual periods in the activity of the radio source. The results obtained with two different methods showed a good correlation between them. For a long time component of the flux the periods of ∼ 5 − 9 years were found. For short term components the periods of ∼ 1 − 4 years are presented. The results obtained using two different methods were compared with VLBI radio maps, which were obtained by the program MOJAVE. The changes of periods over time are associated with certain physical processes in the system "core − accretion disk − jet" and with appearing of new bright components (knots) in the jet.

Keywords: AGN, jet.

1. Introduction

The source 3C 446 is located at the distance 10138 Mpc. It refers to optically violently variable quasars.

Blazar 3C 345 is located at a distance of 3473 Mpc. This source refers to the radio loud quasars. Some authors (eg, Lobanov & Roland, 2005) assume the existence in the source of binary systems of supermassive black holes. In the article (Caproni & Abraham, 2004) the discovery of precession in jet of source 3C 345 is reported.

2. Data reduction

In this paper 3C 446 and 3C 345 are studied. The observations were taken by the radio telescope RT-26 Michigan Observatory, at frequencies of 14.5 GHz, 8 GHz and 4.8 GHz. Graphs of flux density 3C 446 and 3C 345 at three frequencies are presented at Figures 1 and 2. Details of the calibration puethods and the methods of analysis are described in paper (Aller et al., 1985).

Based on daily observations of flux average values of 7 days with an irregular grid of counting are defined. According to the histogram of distribution of time

intervals between counting the interpolation interval in 0.02 years (7,3 days) has been chosen. With using a polynomial moving average (half-width an interval of 5 points) reduction of noise has been reached and random emissions have been removed. By means of trigonometric interpolation the data have been reduced to an even step on time. Allocation of short component in signals against the main period Fourier filtering (O − C) was used (Gaydyshev, 2001).
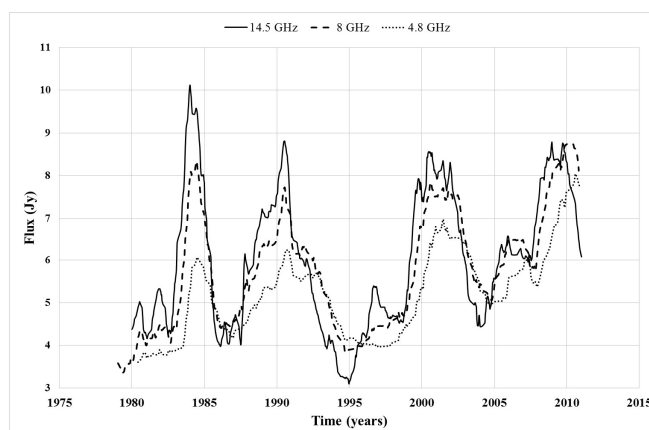

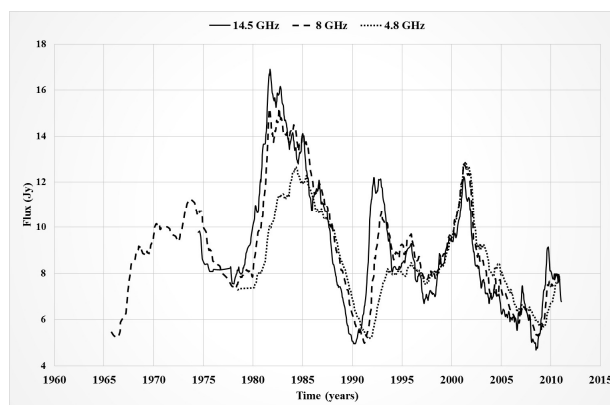Figure 1: A graph of flux density 3C 446 at three frequencies

Figure 2: A graph of flux density 3C 345 at three frequencies

3. Wavelet-analysis

Two-parameter analyzing function of one-dimensional wavelet transform is well localized both in time and frequency. This distinguishes it from the ordinary Fourier analyzing function which covers the entire time axis. Thus, it is possible to see the detailed structure of the process and the evolution of the harmonic components of the signal in time (Smolentsev, 2010). We used a continuous wavelet transform based on Morlet function. On the wavelet spectra of the harmonic components of the signal are visible as bright spots, stretching along the time axis. The examples of the wavelet spectrum are shown in Fig. 3 and 4.
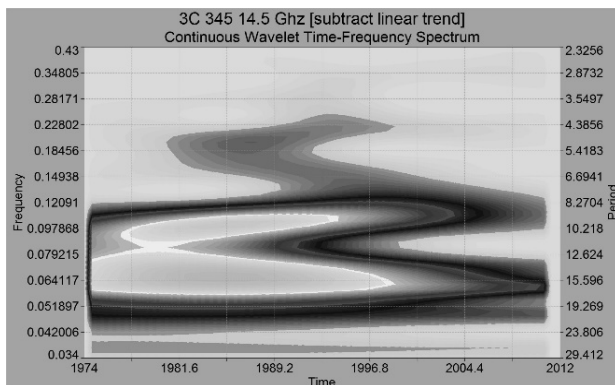

Figure 3: A continuous wavelet-spectrum of the initial smoothed data for 3C 345 at a frequency of 14.5 GHz
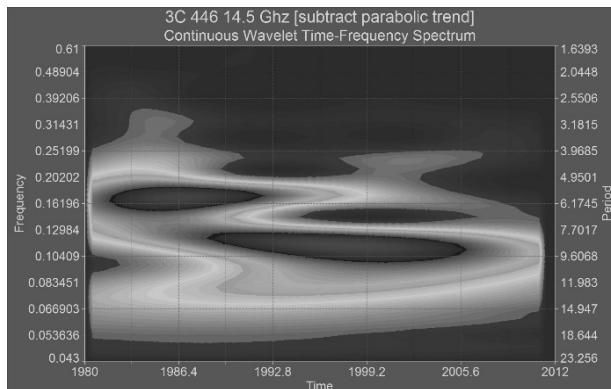

Figure 4: A continuous wavelet-spectrum of the initial smoothed data for 3C 446 at a frequency of 14.5 GHz

Periods and times of the manifestation obtained by wavelet analysis for the sources 3C 345 and 3C 446 are shown in Tables 1 and 2.

At all three studied frequencies for a longtime component of the source 3C 345 the presence of periods in the range of ~ 9 – 12.7 and 16 years is characterized. At frequencies 14.5 and 8 GHz the periods in the range ~ 4.6 – 6.1 years are present. For a short periodic component at all frequencies periods ~ 1.3 – 1.7 and 3 – 4 years are marked. The long ~ 16-year period is marked at all three frequencies and had a maximum of spectral power at 14.5 GHz in 1985, at 8 GHz – in 1988, and at 4.8 GHz – in 1994. The spectral power of 16-year period, was the highest at a frequency of 8 GHz.

Table 1. Periods obtained by wavelet-analysis for 3C 345

Frequency (GHz)	Period (years)	Beginning of the period	End of the period	Maximum spectral power	Date of maximum spectral power
The trend					
14.5	16.4-15.9	1976.8	2004.8	3545	1985.7
	10.5-9.1	1980.2	1998.0	3180	1984.6
	5.3-4.6	1984.4	1991.3	808	1987.5
8	16.1-12.7	1969.6	2007.5	4050	1988.8
	12.7-9.3	1969.6	2004.5	2800	1985.1
	6.5-6.1	1970.4	2000.7	707	1994.8
4.8	16.3-15.9	1984.5	2005.3	3200	1994.6
	9.3-8.7	1983.4	2004.3	890	1992.4
O-C					
14.5	4.0-3.4	1980.4	1999.4	384	1993.0
	1.7-1.5	2001.5	2009.1	46	2008.8
	1.4-1.2	1982.6	1992.3	44	1985.1
8	5.0-4.2	1970.0	2003.4	188	1995.0
	2.7	1971.1	1983.5	42	1976.6
	3.0	1990.1	2007.8	118	1994.2
	1.3	1979.0	1986.0	34	1981.8
	1.7-1.3	1968.2	1975.1	7	1970.5
4.8	4.0	1979.1	2006.0	32	2002.7
	1.3	1981.8	1986.2	8	1984.3

Table 2. Periods obtained by wavelet-analysis for 3C 446

Frequency (GHz)	Period (years)	Beginning of the period	End of the period	Maximum spectral power	Date of maximum spectral power
The trend					
14.5	5.8	1981.7	1995.2	1037	1986.7
	8.8	1997.6	2008.4	1092	1998.6
8	6.0	1981.4	1994.0	343	1986.2
	9.2	1997.0	2008.6	808	1998.8
4.8	5.8	1983.0	1993.7	114	1986.9
	9.2	1996.7	2009.0	407	2000.1
O-C					
14.5	3.0–2.7	1981.0	1998.5	175	1983.6
	2.0–1.3	1988.5	2001.8	32	1990.1
	2.1–1.9	2005.5	2010.3	10	2009.0
	0.8	2000.4	2005.6	7	2001.2
8	2.4–2.1	1980.8	1989.8	8	1983.5
	1.7	2002.5	2009.2	7	2008.4
	1.7–1.1	1988.7	1995.3	4	1991.9
4.8	2.7–2.4	1985.6	2008.7	7	2006.8
	1.4–1.2	1998.8	2008.3	0.7	2000.0

For a long time component of the source 3C 446 at all three frequencies by the presence of periods of 6 and 9 years is characterized. For a short time component at all frequencies the long 6-year period had a maximum of spectral power in 1986. The spectral power of this period was the highest at a frequency of 14.5 GHz. Another long ~ 9-year period had a maximum of spectral power at frequencies of 14.5 and 8 GHz in 1998, and at a frequency of 4.8 GHz – in 2000.

4. "Period – spectral power" dependence

As a result of the wavelet analysis "period – spectral power" graphs were build for each year of observation. They allow to define the periods, making the largest contribution to the formation of phase of activity of the investigated source and the time and duration of their existence.

To study the structure of radio sources in the periods of maximum activity, the VLBI maps from the database MOJAVE for the period 1995 -2012 at the frequency of 15.4 GHz (Lister et al., 2009) were investigated.

Figures 5 and 6 show examples of "period – spectral power" dependence graphs for long term and short-term components of source 3C345 during one phase of its increased activity in 2001 (see. Figures 5 and 6). From these graphs we learn that at this time the periods of ~ 9.2 and 16 years (trend), and the period of ~ 1.7 years (O-C) are seen.
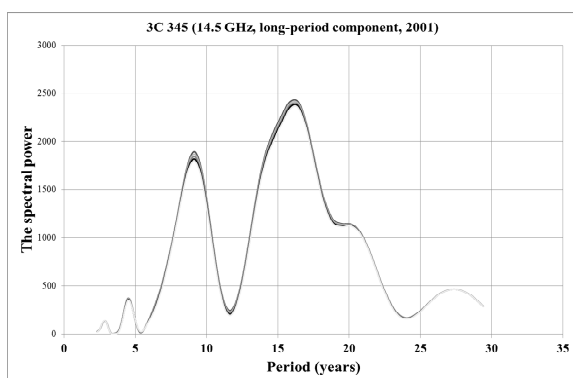

Figure 5: "Period – spectral power" dependence graph for phase of activity for the source 3C 345 in 2001 at a frequency of 14.5 GHz (trend component).
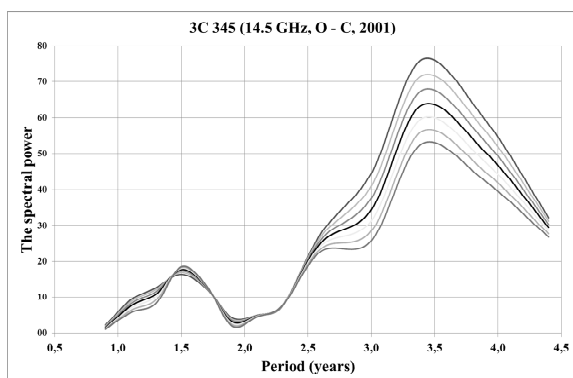

Figure 6: "Period – spectral power" dependence graph for phase of activity for the source 3C 345 in 2001 at a frequency of 14.5 GHz (O-C component).

At the VLBI maps (MOJAVE) for that epoch of observations structural changes in the jet 3C 345 are visible (see. Fig. 7).
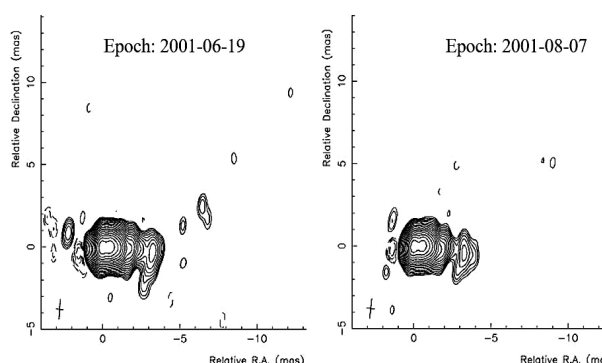

Figure 7: VLBI maps of the source 3C 345 during one of its phases of activity.

Figures 8 and 9 show "period-spectral power" graphs for the source 3C 446 in the phase of its increased activity in 2008. At this time the periods ~ 8.7 years (long-period) and ~ 1.9 years (short-period) are presented. The VLBI maps MOJAVE for this epoch of observations are shown in Figure 10.
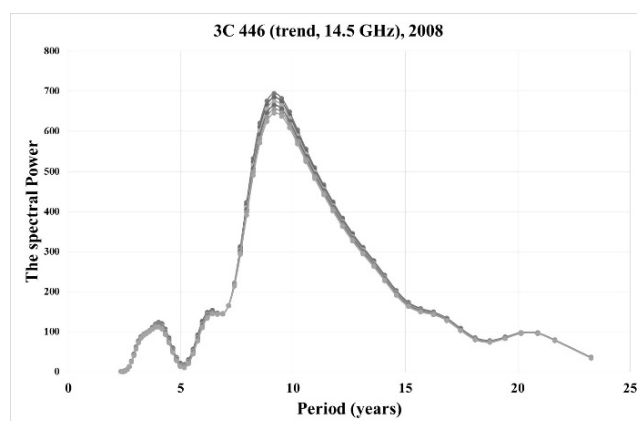

Figure 8: "Period – spectral power" dependence graph for phase of activity for the source 3C 446 in 2008 at a frequency of 14.5 GHz (trend component).
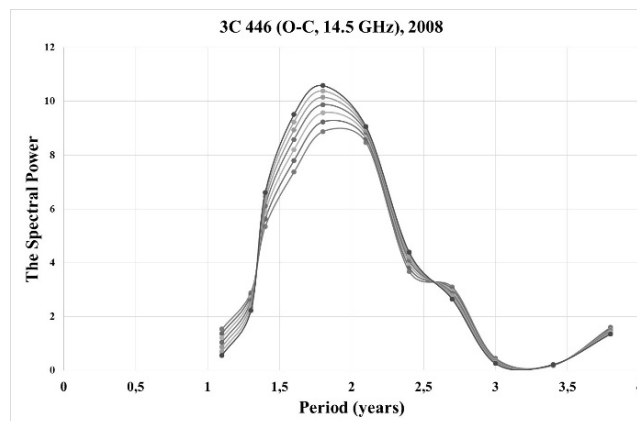

Figure 9: "Period – spectral power" dependence graph for phase of activity for the source 3C 446 in 2008 at a frequency of 14.5 GHz (O-C component).
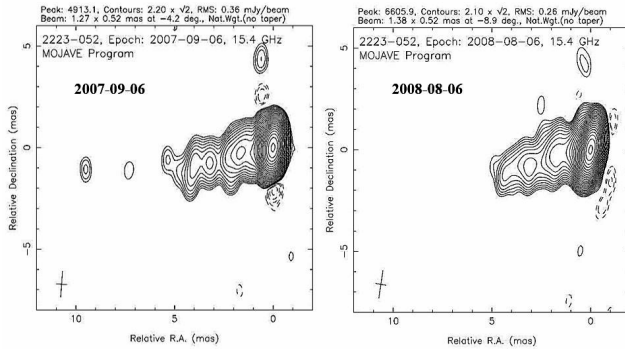
Figure 10: VLBI maps of the source 3C 446 during one of its phases of activity.

5. Singular spectrum analysis

Using the singular spectrum analysis we decompose the original signal into a set of narrow-band filters, which include trend components, periodic components and noise signal (Alexandrov, 2006). Using this set of narrow-band filters, the periods of sinusoidal oscillations in years were determined. To obtain spectral power distribution depending on time in study narrowband component obtained by analysis of a singular spectrum short Fourier transform was used, i.e. Fourier transform used a moving window where each window with overlaps calculated Fourier spectrum and as a result we get a step by step presentation of the temporal evolution of the spectral power and the frequency of the signal. Thus, it is possible to relate the formation of a certain period of time with the moment in which it was the highest. Examples of the obtained principal components are shown in Figures 11 and 12. The eigentriples (principal components) with the numbers 2 – 11 correspond to the required harmonics, and the eigentriples with numbers equal to or greater than 12 are noise.
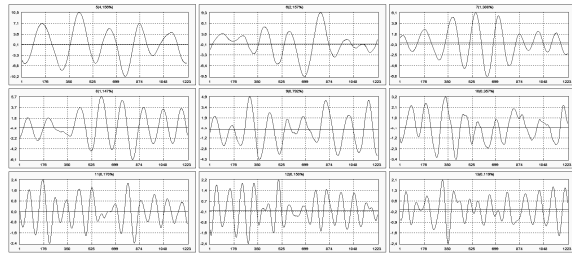

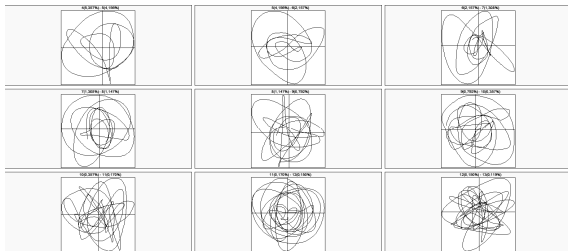Figure 11: The principal components for 3C 345 at 14.5 GHz (one- dimensional diagram)

Figure 12: The principal components for 3C 345 at 14.5 GHz (two-dimensional diagram)

The main drawback of methods with the analyzing function such as Fourier or wavelet analysis is that there is some test function used for comparison with the original series. Singular spectrum analysis allows to avoid the test function, so its calculations allow us within high accuracy distinguish various components of the test series.

Periods for sources 3C 345 and 3C 446 obtained by singular spectrum analysis are shown in Tables 3 and 4. The dates of maximum activity are the same for several periods are typed in bold.

Table 3: Periods obtained by singular spectrum analysis for 3C 345.

Frequency 14.5 GHz		
8.1	2(18,34%), 3(6,80%)	**1983.4**, 1984.3, **1987.8**, 1993.1
6.1	4(5,36%)	1982.4, 1985.8
4.9	5(4,16%)	**1987.9**, 2001.1
4.1	6(2,16%)	**1983.8**, **1996.9**, **2000.7**
3.5	7(1,31%)	**1983.6**, **2000.2**
3.1	8(1,15%)	**1987.4**, **1989.6**
2.7	9(0,79%)	**1987.9**, **1997**
2.4	10(0,36%)	**1987.2**, **1989.6**, **2007.8**
1.7 – 1.9	11(0,17%), 12(0,15%)	**1983.4**, 1988.1, **1989.9**, **1997.3**, **2000.7**, **2007.8**, 2008.5
Frequency 8 GHz		
15.1	1(27,94%),2(25, 73%)	1977.8, **1981.3**, 1984.9, 1987.9, 1992.7
10	3(12,36%), 4(6,33%)	1989.6, **1995.2**, **1997**, 2001.7
6	4(6.33%), 5(3,23%), 12(0,17%)	**1981.5, 1995.2**, **1995.9 1998.6**, 2000.8, 2001.7
4.3	6 (1,498%)	1997.95
3.3 – 3.8	7(1,28%), 8(1,16%), 11(0,44%),12(0, 17%)	**1972.8**, **1981.5**, 1983, 1989.8, 1991.6, **1997.6**, **1998.6**, **2002.6**
2 – 2.7	9(0,78%), 10(0,62%), 12(0,17%)	**1972.9**, **1981.5**, **1998.4**, **2002.6**
Frequency 4.8 GHz		
Period (years)	**Principal components**	**Date of maximum activity**
4.3	5(1,85%), (1,20%)	1985.4, **1987.9**, 1999.1, **2000.9**
2.7	7(0,73%), (0,56%), 9 (0,22%)	**1998.3**, **2000.9**, **2001.1**, 2004.9, **2006.6**
1.8 – 2.2	9(0,22%),10(0,2 0%), 11(0,19%),12(0, 15%)	**1998.5**, **2000.5**, **2006.5**

Table 4. Periods obtained by singular spectrum analysis for 3C 446.

Frequency 14.5 GHz		
10.4	1(27,62%), 2(25,24%)	**1984.6**, 1988.8, **1992.9**, 1994.7, 2004.6
5.2	3(16,12%), 4(8,88%)	**1983.1**, **1984.7**, 1994.1, 1996.1
4.1	5(2,99%), 8(0,74%)	**1983**, **1989.1**, **1992.6**, 1995.2, 2000.8, **2006.9**
2.6 – 3	6(2,14%), 7(1,88%), 8(0,74%)	**1983**, **1985**, **1989.1**, **1992.6**, 1995.8, 1998.7, 1999.9, **2006.9**, 2007.1
2.3	9(0,35%)	2000.3
1.7 – 2	10(0,28%), 11(0,25%), 12(0,24%)	**1983.1**, **1984.6**, **1985**, **1985.2**, 1985.9, 1989.9, **1992.6**, 2005.3
Frequency 8 GHz		
10.6	1(28,00%), 2(26,22%)	1996.7, **2000.9**
5.3	3(13.41%), 4(7,64%), 6(1,87%)	1983.2, **1983.9**, **1990.4**, **2000.7**, **2009.7**
4.25	5(3,95%), 8(0,85%)	**1983.8**, **1985.5**, **1990.4**, **1995.9**
2.7 – 3	6(1,87%), 7(1,52%), 8(0,85%), 11(0,23%)	**1983.9**, **1985.6**, **1990.3**, 1991.9, 1994.5, **1995.9**
1.9	9(0,41%), 10(0,38%)	**1985.3**, **1990.9**, 1992.1, **1995.9**, **2009.7**
1.5	12(0,17%)	**1983.9**, **1995.8**
Frequency 4.8 GHz		
Period (years)	**Principal components**	**Date of maximum activity**
10.2	1(30,61%), 2(29,51%)	**1995.6**, **1998.9**, **2000.8**, **2006.2**
5.1	3(9,38%), 6(0,88%), 7(0,70%), 8(0,56%), 11(0,14%)	**1983.7**, **1984.8**, **1995**, **1995.7**, **1997.4**, **2001.4**, **2007.2**
4.1	4(4,18%), 5(2,15%)	1985, **1993.9**, **1994.3**, **2000.6**, **2001.5**, 2004.6
2.6 – 2.9	6(0,88%), 7(0,70%), 8(0,56%), 11(0,14%)	**1983.7**, **1984.8**, **1994.9**, **1995.3**, **1997.4**, **2001.6**, **2007.2**
2	9(0,29%), 10(0,28%)	**1993.9**, **2000.4**
1.6	11(0,14%), 12(0,10%)	1985.8, **1995.6**, **1998.6**, **2001.8**

The common manifestation of several periods at the same time corresponds to maximum amplitude of flux.

Summary

We investigated the data of monitoring of flux density of extragalactic sources 3C446 and 3C345, which was held on 26-meter radio telescope of University of Michigan at frequencies 14.5, 8 and 4.8 GHz. The data of observations were investigated using singular spectrum analysis.

In investigated sources trend components were found in the range ~ 6 – 10 years (3C345) and 5 – 9 years (3C446). Short-component is characterized by manifestation of periods ~ 1.2 – 5 years (3C 345) and 0.8 – 3 years (3C 446). It is assumed that the long-period components correspond to the core activity, and short-components correspond to structural changes in the jet. Data analysis was carried out by two supplementing each other methods: wavelet analysis and singular spectrum analysis. Wavelet analysis is based on the Fourier transform, while the singular spectrum analysis does not use the analyzing function. The results of calculations of the singular spectrum analysis of fluxes of extragalactic sources were compared with the results of the wavelet analysis. The results obtained with two different methods showed a good correlation between them. The obtained data were compared with the VLBI maps (database MOJAVE) to study the evolution of component in the jets of the quasars studied. There was found the relationship of manifestation of certain periods of variability with changes in the jet.

References

Alexandrov F.I.: 2006, Development of software system for automatic selection and forecast of additive components of time series in the framework of the "Caterpillar SSA", Publishing House of St. Petersburg State University.

Aller H.D. et al.: 1985, *ApJS*, **59**, 513.

Caproni A., Abraham Z.: 2004, *Proc. of the International Astronomical Union*, Issue IAUS **222**, 83.

Gaydyshev I.: 2001, *Analysis and data processing (the special directory)*, St.Petersburg Publishing house.

Lister M.L. et al.: 2009, *AJ*, **138**, Issue 6, 1874.

Lobanov A.P., Roland J.: 2005, *A&A*, **431**, N 3, 831.

Smolentsev N.: 2010, *Veyvlet-analiz in MATLAB*, DMKPress.

MONITORING THE COMMUNICATION CHANNEL FROM PUSCHSHINO TO MOSCOW IN THE PROJECT OF SPACE RADIO TELESCOPE "RADIOASTRON"

D.V. Dumsky[1,2], E.A. Isaev[1,2], V.A. Samodurov[1,2], K.A. Isaev[3]

[1] P.N. Lebedev Physical Institute, RAS,
53 Leninskiy Prospekt, Moscow, 119991, Russia, *dumsky@prao.ru*

[2] National research university Higher school of economics, *is@itaec.ru*
Moscow, 101000, Russia

[3] Institute of Mathematical Problems of Biology, RAS,
4, Institutskaja str., Pushchino, Moscow Region, 142290, Russia

ABSTRACT. The need for transmission and storage of large amounts of scientific data in the project space radio telescope "Radioastron" required us to organize a reliable communication channel between the tracking station in Pushchino and treatment centers in Moscow. Network management data requires us to an integrated approach and covers the organization secure access to manage network devices, timely replacement of equipment and software upgrades, backups, as well as documentation of the network infrastructure. The reliability of the channel is highly dependent on continuous monitoring of network and server equipment and communication lines.

Keywords: Radioastron; monitoring; telecommunications.

located at the radio observatory near Puschino, outside of Moscow (Fig.1). Flow of digital data received by tracking station can reach 128 Mbit/s. For efficient data exchange the direct communication fiber channel between PRAO and processing center ASC FIAN was created. The capacity of channel is 1Gbit/sec. In addition to tracking station the buffer data-center created as a reference node communication and file storage accomodation. The scientific data channel is used for transmission of telemetry information from the board of the spacecraft too. The channel of communication provided by ISP with guarantee of redundancy via two independent optical lines, and organized using technology MPLS (Multiprotocol Label Switching).
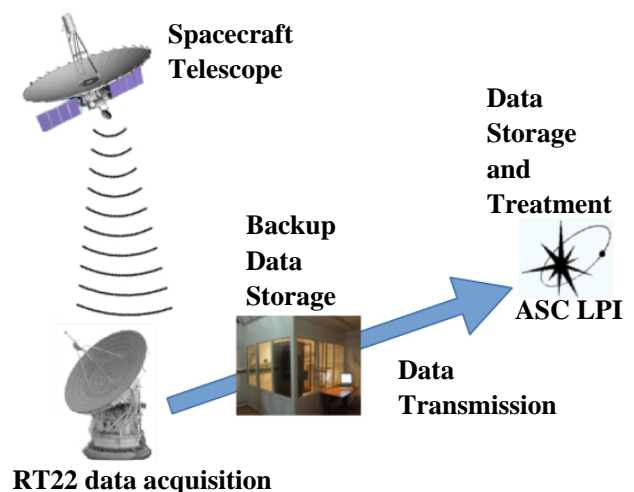
1. Introduction

The RadioAstron is an international space VLBI project led by the Astro Space Center of Lebedev Physical Institute in Moscow, Russia. The payload - Space Radio Telescope, is based on spacecraft Spektr-R, that have been designed by the Lavochkin Associations. The purpose of the project is to use the space telescope for radio astronomical observations using VLBI (Very Long Baseline Interferometry) techniques in tandem with ground-based VLBI networks located in Australia, Chile, China, Europe, India, Japan, Korea, Mexico, Russia, South Africa, Ukraine, and the USA. The scientific objective of the project is to produce an image coordinate measurement and angular movements of different celestial radio sources with extremely high angular resolution (Kardashev et. al., 2012, Kanevskiy et al., 2014).

Ground tracking support of the spacecraft is currently provided using the 22-m antenna (RT-22)

Figure 1: Radioastron data chanells.

2. Chanell monitoring

Failsafe operation of the communication channel is especially relevant for the space telescope. For example, uninterrupted reception of telemetry data allows specialists to take further decisions on the correction of its orbit and receive important information about the performance of the onboard equipment. The success of the scientific experiments directly related to the reliability of the transmission of scientific data. This requires solutions that can automatically detect and respond to threats and channel performance issues in real time, as well as predict possible issues in the future. Monitoring system gives us the opportunity to have the right information about data transmission at the right time.

Real-time monitoring of hundred of metrics collected from network devices and servers is an important prerequisite for the smooth operation of the scientific data channel and the equipment in its structure. Monitor of availability, syslog messages, power consumption, temperature conditions and other various aspects of equipment performance help us maintained overall performance of the channel at an acceptable level. The main features of monitoring system is alerts when a fault occurs and storage of events history in DB.

We choose Zabbix as monitoring system because it is easy to use, it is Open Source and met most of the requirements we had for a monitoring tool in our environment for channel maintenance (Dumsky et al., 2014). The monitiring system is a powerful network tool that helps us to ensure that critical systems, applications and services are alwaysup and running. It must provides features such as alerting, event handling, reporting and performance statistics. With items collecting data and triggers designed to "fire" upon problem situations, we have alerting mechanism in place that is notify us about important events by email even when we are not directly looking at Zabbix frontend panel. We can see in which of the sites of the channel detects a problem with the help of interactive map monitoring in real-time. The current values of monitored parameters, as well as their changes can be viewed as separate graphs with scale changes by the hour, day, week and month (Fig.2).

2. Conclusion

Every day about 50 to 300 GB of unique information about the structure and evolution of various astrophysical objects (blazars, pulsars, cosmic masers and black holes) is transmitted through the channel. The same amount of data backed up in the PRAO ASC LPI buffer data storage. The average data rate of the channel transmission is typically 300-400 Gbit/s.
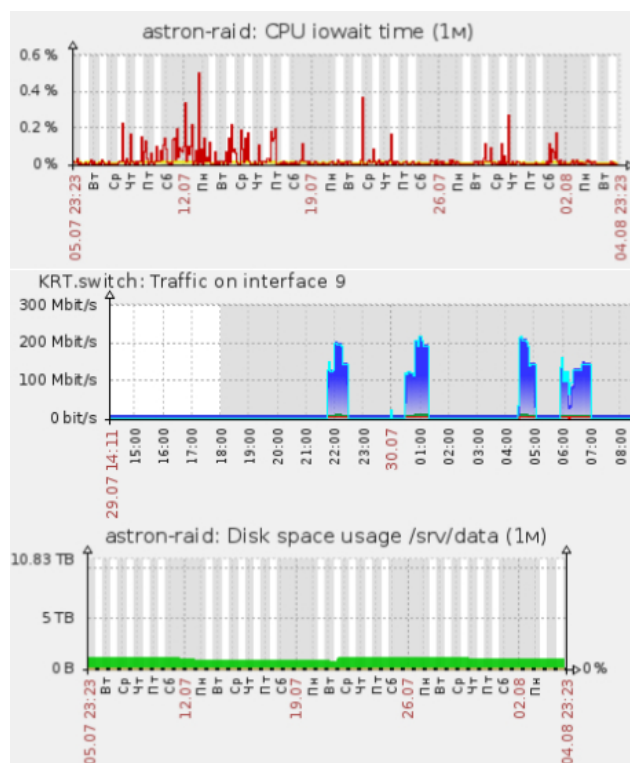

Figure 2: Graphs of important channel parameters.

The monitoring system over the past two years, allows us quickly resolved emergency situations caused by the power failure and failures of the network equipment, and cooling system of the buffer data center, as well as identify the causes of failures of channel associated with the failure of the individual switching devices and optical modules. We were promptly detected and eliminated two cases of the optical lines damage, allowing to minimize the idle time of the channel work. Monitoring of disks in buffer storage allows us for timely replacement of failed drives, that would prevent the destruction of RAID-array and prevent permanent loss of scientific data.

References

Kardashev N.S., Kovalev Y.Y., Kellermann K.I.: 2012, *The URSI Radio Science Bulletin,* **343**, 22.

Kanevskiy B.Z. et al.: 2014, *Bulletin of S.A.Lavoshkin Federal Research and Production Association,* **3**, 47.

Dumsky D., Isaev E., Samodurov V.A. et al.: 2014, *Odessa Astron. Publ.,* **27**. 71.

SECULAR DECREASE THE FLUX OF SUPERNOVA REMNANT CAS A ON MONITORING RESULTS TO RADIOTELESCOPE "URAN-4" IRA NASU

A.A.Gorbynov[1], M.I.Ryabov[2], S.K.Panishko[2]

[1] Astronomy Department of I.I.Mechnikov Odessa National University
[2] Odessa observatory "URAN-4" of the Institute of Radio Astronomy NASU

ABSTRACT. This work is dedicated to the study of secular decrease of the flux of young supernova remnant Cas A according to observations by radio- telescope "URAN-4» of Odessa Observatory IRA NASU from 1987 to 2001 years on frequency of 25 MHz. On the investigation base there is a relationship analysis of flux CasA to the "stable" source – radio-galaxy Cyg A (CasA/Cyg A) which is located on a small angular distance. Results of the observations held on RT «URAN-4» show that there is no noticeable decrease of fluxes in the period 1987-1993, with the relationship ratio (CasA/Cyg A) = 1.5. While considering data from 1987 to 2001 manifested a slight decrease trend in flux equal to 8.4% for the all period. At the same time, according to various investigations the average value flux of Cas A in the interval of frequencies 38-2924 MHz is 0.8% per year. At the meantime in this frequency the range ratio (CasA/Cyg A) has become less than one. Thus, there is a noticable contradiction of secular decrease of the flux Cas A on this radio frequencies in comparison with the predictions of the theory in 1.7% per year.

Keywords: supernova remnant, radioemission.

Introduction

In 1948 British radioastronomers Riley and Smith discovered an extremely bright radio source in the constellation Cassiopeia. They named it Cassiopeia A. This source became calibration for the majority of radio astronomy catalogs. It soon turned out that the flux varies systematically. The reason for these changes is the expansion of the supernova remnant. The theoretical explanation of the expansion of the supernova remnant was represented in the work of Shklovskii (1960).

Result of multifrequence observations

Observations of Cassiopeia A flux changes were at different wave lengths. At shorter wave lengths dominated secular decrease in flux. At longer wave lengths decrease flux was less noticeable. At the same time, at longer wave lengths we observed episodic change of flux associated with the state of the ionosphere.

Carrying out absolute changes of fluxes of radio sources is due to technical difficulties with their organizing and observations. In this regard the determination of flux changes of Cas A is considered its relation to the flux of the radio galaxy Cygnus A (Cyg A) that is located on a small angular distance. This ratio is recorded as Cas A/Cyg A.

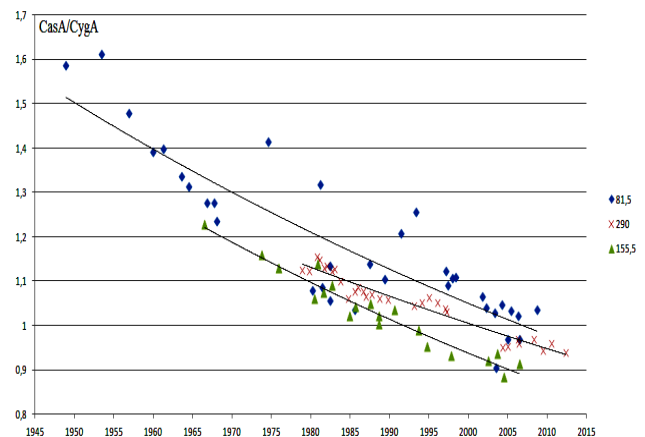The results of such measurements at frequencies of 81.5, 151.5 and 290 MHz are shown in Fig. 1.

Figure 1: The ratio of fluxes Cas A / Cyg A at frequencies 81.5, 151.5 and 290 MHz.

Studies have been conducted at certain frequencies, indicated in the figures. One of the conditions is the stability of the radiation Cyg A. As a result, the rate d_v was obtained - secular decrease of the flux density of the radio emission in Cas A (Vinyakin, 2014).
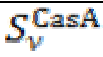
$$d_{81.5}(2005.0)= 0.71 \pm 0.06 \text{ \% year}^{-1}$$

$$d_{151.5}(2005.0)= 0.78 \pm 0.04\text{\% year}^{-1}$$

$$d_{290}(2005.0)= 0.61 \pm 0.03\text{\% year}^{-1}$$

Nick Rees (1990) has studied the relationship Cas A/Cyg A. He found anomalous behavior relationships CasA/Cyg A at a frequency 38MHz (Rees, 1990). Such a deviation requires a detailed study on a longer period of time. Studies have been conducted on the meter and decameter waves. We found four periods in the spectrum of variations relationships Cas A/Cyg A: (3.1 ± 0.02); (5.1 ± 0.3); (9.0 ± 0.2) and (24 ± 2) years. If the flux Cyg A is constant, they can be attributed to the secular variation Cas A.

According to various studies, the average decrease of flux Cas A in the frequency range 38-2924 MHz is detected in interval 0.39-0.99 % per year (see Table 1) (Bovkoon, 2010; Vinyakin, 2014).

Table 1:

v	Epoch measurement	$-dv$(2005), % year^{-1}	S_v^{CasA} (2015.5), Ян
20 MHz	1984.5	0.71 ± 0.12	37265 ± 3120
25 MHz	1984.5	0.99 ± 0.09	32095 ± 1890
38 MHz	1980.1	0.73 ± 0.13	26540 ± 2015
927 MHz	1991.2	0.68 ± 0.03	2360 ± 140
2924 MHz	1983.2	0.50 ± 0.09	1038 ± 64
22680 MHz	2005	0.51 ± 0.01	219.7 ± 3.0
32940 MHz	2005	0.55 ± 0.02	169.4 ± 1.8
33000 MHz	2002.9	0.39 ± 0.02	171.6 ± 0.6
40620 MHz	2005	0.56 ± 0.02	144.6 ± 1.7

Currently, as a result of the secular decrease of flux Cas A over frequency intervals 38 MHz ratio of the fluxes Cas A / Cyg A was less than one. Thus, there is a noticeable difference in the magnitude of the secular decrease in flux Cas A on radio frequencies than the theoretical predictions of 1.7% per year.

Observations on radiotelescope «Uran-4»

Observation Cas A on radiotelescope "URAN-4» of Odessa Observatory IRA NASU have been held for monitoring programme of fluxes of powerful radio sources at a frequency of 25 MHz since 1987 till present time. The study is based on analysis of the ratio of the flux to the Cas A "stable" source - radio galaxy Cyg A (Cas A / Cyg A).

In 1987-1993 observations were conducted in analog regime registration during 10-14 days a month. In 1999-2014 observations were carried out continuously in digital regime registration.

The procedure for processing the observation data was the following:

1. Flux of radio emission of the source was determined in relation to the power calibration signal noise generator.

2. The effective area of the antenna in different hour angles is different.

Therefore, the data obtained in different hour angles cited to the direction of the culmination radio source.

3. Matrix of observation data was processed to detect accidental releases. After their exclusion, we determined the average daily values, average for the entire period of observation and their dispersion.

Results of observations on RT «Uran-4»

According to observation results it has been found that for a correct consideration of changes of fluxes Cas A / Cyg A it is best to divide into two intervals of data. The first interval includes observations from 1987 to 1993 (Fig.2).
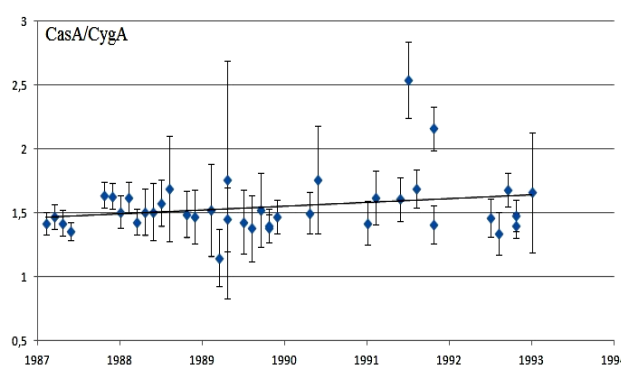

Figure 2: Observations of flux ratio Cas A / Cyg A from 1987 to 1993.

The results of observations carried out at RT "URAN - 4", show no appreciable drop in fluxes between 1987 and 1993 when the value of the flux ratio (Cas A / Cyg A) = 1,5.

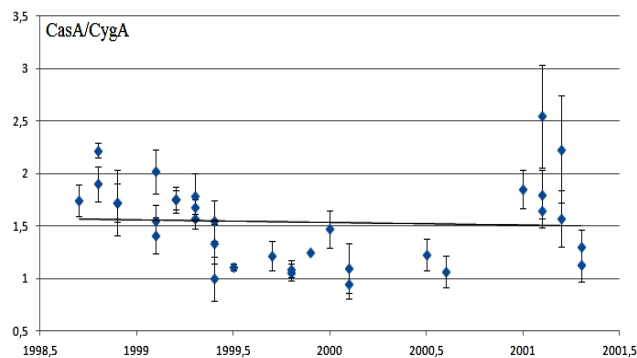The second period includes observational data from 1998 to 2002 (Fig. 3).

Figure 3: Observations of flux ratio Cas A / Cyg A from 1998 to 2002.

When considering the data from 1987 to 2001, there is a tendency of the flux decreasing, equal to 8.4% over a period of 14 years.

Conclusion

As a result of observations on the RT Uran-4 we received a marked contrast of the flux changes of Cas A at a frequency of 25 MHz compared to higher frequencies. The results of observations carried out at RT "URAN-4", show no appreciable drop in fluxes between 1987 and 1993 when the value of the flux ratio (Cas A / Cyg A) = 1,5.

The reason of regime change from the stability to reducing the flux of Cas A at decameter wavelengths may be the existence of a compact component in the center, especially the angular structure of the residue found in the X-ray space telescope "Chandra" and variations of the state of the ionosphere in the changing solar and geomagnetic activity. This can be quite a strong modulation of the flux of source, due to the influence of solar activity and seasonally-day effects. Hence, for solving the problem of secular decrease of Cas **A** radio flux at low frequencies, the season-day effect determined by observation should be taken into account. This effect results in scatter of the ratio *3C461/3C405* within the range *1.3-1.7* and enhanced dispersion if one or both sources are observed through non-stable ionosphere (Ryabov, 1993).

When considering the evolution of the flux of Cas A it should be taken into account: the existence of a compact source in remnant, rupture of the shell, the lifetime of individual condensations, the presence of shock waves in the remnant, modulation of the flux under the influence of changes in the state of the ionosphere. All this will help to better understand the processes that occur in the evolution flux of Cas A on the radio waves. In this regard, it is likely variability of Cyg A flux due to these effects will study in the future.

References

Rees N.: 1990, *R. Astron. Soc.*, **243, 637.**
Bovkoon V.P. et al.: 2010, *Radiophys. and Radioastron*.
Ryabov M.I. et al.: 1993, *Astron. and Astrophys. Trans.*, **4**, 29.
Shklovsky I.: 1960, *AJ*, **37**, No2, 256.
Vinyakin E.N.: 2014…91, 9, 720.

LIGHT CURVE TYPES OF CLASSIC T TAURI STARS

N.Z.Ismailov, H.N.Adygezalzade

Shamakhy Astrophysical Observatory after named N.Tusi of ANAS
AZ 5626, Y.Mamedaliyev set., ShAO, Shamakhy, Azerbaijan, *ismailovn@yahoo.com*

ABSTRACT. By using the archive photometric data's obtained for a long time intervals we have carried out a master light curves of 28 classical T Tauri type stars. For the physical character of variability mainly 5 type light curves can be separated. We have proposed a new scheme of classification among the examined light curves. The proposed scheme suggests a qualitative interpretation in terms of interaction of the central star with its circumstellar accretion disk.

Keywords: T Tauri stars, variability, master light curves, classification.

1. Introduction

T Tauri stars were first identified as an interesting pre-main sequence class of objects because of their unusual spectral and photometric properties (Joy, 1945, Herbig, 1962). Classical T Tauri stars are possess strong emission lines (hereafter CTTS) (stars with equivalent widths W(Hα)≥10Å) and are now recognized as pre-main sequence stars accreting material from an extended circumstellar disk. There are also T Tauri stars (hereafter TTS) with weak emission lines and circumstellar disk indicators (so-called "weak-line" TTS: WTTS) or without emission lines and disks (hereafter naked TTS: NTTS). Despite a large amount of observational material obtained for last 60 years, there remains unclear a physical causes of the light variations of TTS.

Researches of last year's show that there are only a rather limited number of plausible mechanisms by which a star could conceivable change its apparent brightness. At this time such mechanisms were proposed: 1) the rotation of the star with an asymmetrical distribution of cool spots, 2) variable hot spots on the stellar surface, 3) stellar flares and accretions, 4) grows and decay of large active regions on the photosphere and, 5) obscuration by circumstellar dust (e.g., Herbst et al.,1994).

The classification scheme for "Orion variables"— now called T Tauri stars — firstly suggested in 1954 by Parenago (1954) based on photographic observations is still relevant today. In this scheme, the most important factor is the shape of the light curve. Following Parenago's (1954) scheme Herbig (1962) classified the forms of light curves into four classes. Then Herbst et al.(1994) were divided TTS light curves into four types based on the color and spectral variations.

The relationship between Herbig's "class" and Herbst et al.'s "type" is not clear, but may reflect the different time scales of variability, i.e., longer for the "class" (10-100 days) and shorter for the "type" (0.5-30 days). Moreover, both proposed classification schemes make difficulties in separation of the different type of light curves. Our purposes in this report are consideration of the forms of CTTS light curves obtained on the more rich observational data.

2. Observational data and results

We used the photoelectric *UBVRI* observation results from the Wesleyan University database (ftp://sun.astro.wesleyan.edu) (Herbst et al.1994) and from archive Grankin et al. (2005) which is a collection of many-year observations by various authors. These data do not cover all available observations for individual objects, but the amount of material is sufficient to study the general characteristics of the T Tauri stars represented in the database. To avoid biases due to observational selection effects, we chose objects with as many data points as possible accumulated over decades. Moreover we included to this material for some stars results from ASAS database (www.astrouw.edu.pl/asas) for *V* and *I* bands.

We selected a total of 28 classical T Tauri stars with more than 300 observations as a minimum in various filters. The typical photoelectric photometry uncertainties are about ± 0.01^m in *B* and *V* and, as a rule, no more than ± 0.03^m in *U*. For the ASAS data average uncertainties is relatively large (at ± 0.05^m), while we have not discovered some systematic differences with data's from other catalogues. We were not able to correct for systematic differences between the data of different authors, but most of the observations for individual stars appear uniform, indicating that such systematic differences are not significant. İn the Figure 1 demonstrated plotted master light curves of some CTTS.

After plotting the light curves for all 28 stars, we attempted to identify general tendencies and differences among these curves. Figure 2 displays an example of each of the light curve types we found among the T Tauri stars in our sample. The arrows in Figure 1b schematically explain our approach to estimating the amplitudes of brightness variations for (i) active states with high amplitudes (ΔV_1) and (ii) quiet states with low amplitudes (ΔV_2), at approximately the same brightness level. A list of selected objects, amplitudes ΔV_1 and ΔV_2, full amplitudes of color indexes Δ(U-B), Δ(B-V) and determined types on our classification scheme are presented in the Table 1.

Both existing photometric studies of T Tauri stars and our results show the following common features in the light curves. All the T Tauri stars display irregular brightness variations over several days during various observing seasons. The stars show both quiet and active

states. In the quiet state, the daily brightness variations (we will use this term to refer to all brightness variations with time scales within 1–15 days) for individual stars can have amplitudes from 0.07^m to 1.6^m (V866 Sco), but, in most cases, the V amplitude is within 1^m.

Rapid daily brightness variations are observed in both the active and quiet states. The amplitudes of the brightness variations in the active and quiet states, ΔV_1 and ΔV_2 (Fig. 1b), differ, with their ratio being almost constant, on average higher than two.

We determine the active and quiet states of a star as follows. As a rule, during a given time interval, a star displays brightness variations that can be described with two parameters: the mean brightness and the amplitude of the daily variations. Both parameters can differ considerably from season to season. To study these variations, we selected the extreme states of both parameters. Thus, we can characterize the states of the highest and lowest mean brightness. We call these extreme states of the amplitude of the daily variations the star's "active" and "quiet" states. The star's mean brightness in its active and quiet states can be different or virtually the same.
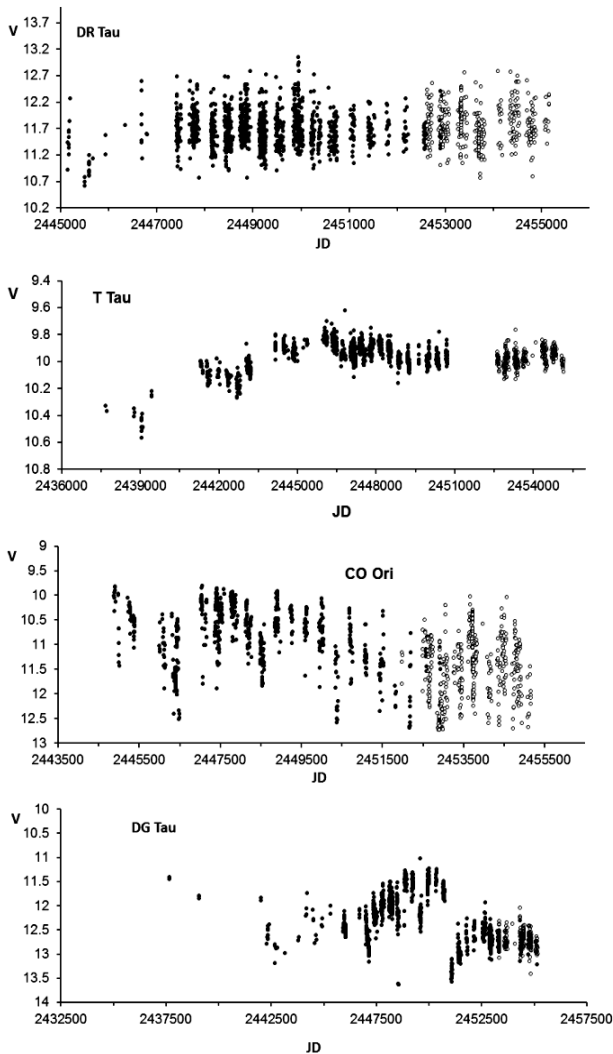
Our analysis shows that we can clearly distinguish five different types of light-curve shapes. We distinguish the following principal types based on light-curve shape:

type I: constant mean brightness without changes in the amplitude of the rapid brightness variability;

type II: constant mean brightness with changes in the amplitude of the rapid variability;

type III: varying mean brightness without changes in the amplitude of the rapid variability;

type IV: variations of both the mean brightness and the amplitude of the rapid variability;

type V: the variable is often bright, and rare brightness decreases (dimmings) are observed.
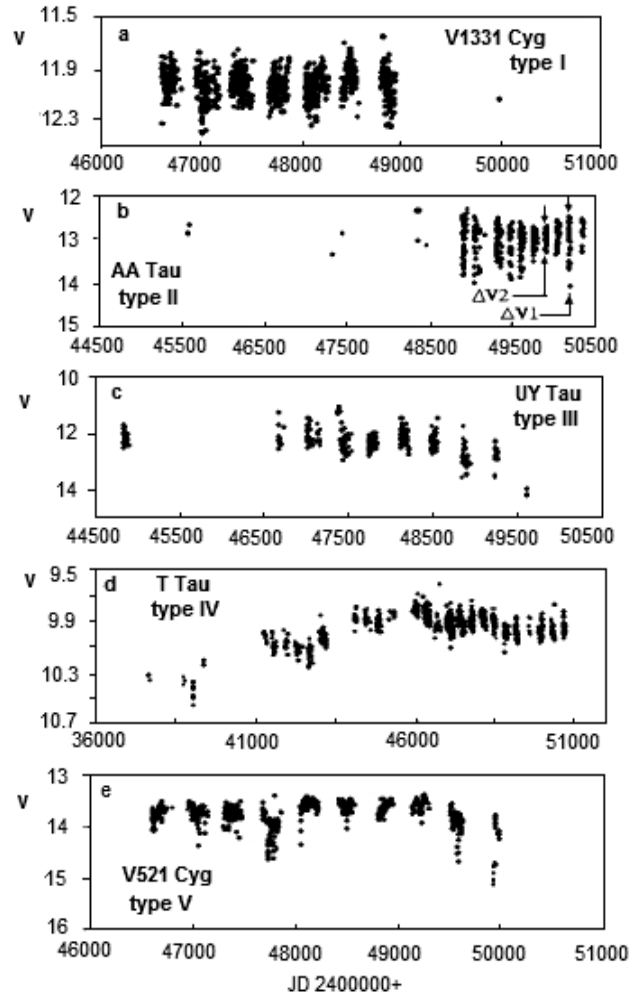

Figure 2: Selected typical examples of CTT light curves. The arrows in panel (b) explain our technique for estimating amplitudes during different brightness states of the stars.

Figure 1: Examples of master light curves for some CTTS. Dark cycles-from catalogue Herbst et al.(1994), open cycles from ASAS database.

Type I stars exhibit brightness variations whose amplitude is almost the same in different years, and whose mean brightness does not vary. Only two stars like this were found in our sample, DL Tau and V1331 Cyg (Fig. 1a). Despite the presence of some scatter about the mean level, the mean brightness itself does not vary. Such variability can be explained by brightness modulation of a cool spot on the surface due to axial rotation of the star. In

this case, we must assume that the spots are very stable and that their relative area does not vary within a season or from season to season.

The mean brightness of the type II stars does not vary, but their rapid variations on time scales of several days are accompanied by gradual changes in their amplitude over several years. Typical representatives of this group are DR Tau and AA Tau (Fig. 1b). This type has the most members in our list (13 stars of 28). Such variations could be due to modulation of the star's brightness in the presence of a hot spot or to variable activity of the star itself, similar to cyclic solar activity, as well as to the appearance of additional radiation associated with non-stationary disk accretion. The light curves of this type suggest that such activity appears and then gradually disappears over five years.

Similar to the type I stars, the type III stars do not show variations in the amplitude of their rapid daily brightness variability; smooth changes of the mean brightness (trends) on time scales of several years are observed. A typical example is DN Tau (Fig. 1c). In our opinion, this type of variability requires the presence of a stellar companion whose brightness is comparable to that of the variable star and comparatively constant. Then, in principle, the brightness variations can be described fairly well using a cool spot model.

In addition to their rapid daily variations, the type IV stars exhibit simultaneous changes in their variability amplitude within a season, as well as long-term changes in their mean brightness over several years. Most ETT stars are of this type; typical representatives are T Tau and RY Tau. It is likely that, along with seasonal changes due to the star's chromospheric activity, eclipses by an invisible companion or a protoplanet also occur (Fig. 1d).

The type V stars are as a rule, in bright condition. There are sometimes rapid daily variations with amplitudes of up to 0.5^m, but abrupt dimmings with amplitudes exceeding $\sim 1^m$ in V are also observed in some years. A typical representative is V521 Cyg. If objects such as this exhibit dimmings often and within short time intervals, then the star's light is probably blocked by circumstellar gas and dust (Fig. 1e).

Table 1. Observational data for the studied sample of T Tauri stars

Star	ΔV_1	ΔV_2	$\Delta(U - B)$	$\Delta(B - V)$	Sp	Type
BM And	2.35	1.04	0.79	0.38	K5V	IIII
RW Aur a	2.66	1.09	0.93	0.69	K1V	IV
SU Aur	1.1	0.17	0.51	0.38	G2III	III
UY Aur	3.18	0.82	1.06	1.61	K7V	II
GM Aur	0.74	0.3	1.36	0.49	K3V	IV
DI Cep	0.57	0.19	0.54	0.37	K1V	V
V521 Cyg	1.77	0.31	0.32	0.47	G8	II
V1082 Cyg	1.05	0.74	0.82	0.4		I
V1331 Cyg	0.73	0.42	0.58	0.12		III
V1121 Oph	0.74	0.45	0.68	0.51	K5	IV
CO Ori	2.68	0.45	0.72	0.37	F8	V
GW Ori	0.63	0.07	0.43	0.23	G5V	II
V866 Sco	3.56	1.6	0.42	0.58	K5V	IV
T Tau	1.1	0.18	0.79	0.26	K1V	IV
RY Tau	1.25	0.23	0.39	0.15	K1IV	V
UX Tau ab	2.13	0.93	0.78	0.51	K2V	II
AA Tau	1.77	0.66	1.5	1.04	K7V	II
BP Tau	1.31	0.19	0.78	1.25	K7V	II
CI Tau	1.51	0.41	1.12	0.49	K7V	II
DF Tau	1.95	0.23	1.8	1.22	M0	III
DG Tau	2.15	0.75	0.36	0.36	M?	VI
DK Tau	1.95	0.23	0.42	0.81	K7V	III
DL Tau	2.02	0.8	0.44	0.69	K7V	IIII
DN Tau	0.55	0.34	0.42	0.18	M0V	II
DR Tau	3.67	1.81	0.74	0.78	K5V	II
GG Tau	0.58	0.15	0.62	0.75	K7V	
GI Tau	2.95	1.39	2.18	1.29	K6V	
GK Tau	1.13	0.68	1.23	0.54	K7V	

3. **Conclusion**

Let us obtain a simple estimate of the accreted mass needed to provide a V-brightness variation of $\Delta V = 0.5^m$, as is typical of most CTT stars (Herbst et al. 1994)

Many photometric observations of T Tauri stars show brightness variations in the quiet phase of up to several tenths of a magnitude. Let the star have a mass and luminosity equal to the solar values (G2V spectrum). A brightness change $\Delta V = 0.5^m$ will then imply an increase of the radiated flux by a factor of 1.58, and the additional flux for such a brightness variation is $\Delta E = 2.2 \times 10^{33}$ erg·s^{-1}. The characteristic fastest motions indicated by the observed emission lines of T Tauri stars (including those related to accretion onto the star) have velocities of about 300 km/s (e.g. Petrov et al., 1999). With such velocities for the accreting matter, the energy balance of the additional radiation flux requires a mass of up to $\Delta M = 4.7 \times 10^{22}$ kg, which is about a factor of 100 lower than the mass of the Earth and is comparable to the mass of the Moon. This demonstrates that the variability of stars having type I light curves (constant mean brightness and constant amplitude) can probably not be due to the accretion of matter from a circumstellar disk, because the rate of accretion onto a star cannot be constant. Type I brightness variations could be due to the presence of a cool spot and/or an active chromosphere

A simple calculation shows that a large mass, comparable to that of the solar system's planets, can fall onto the stellar surface during an outburst, apparently within a short time (days). Such large brightness variations are characteristic of type IV T Tauri stars. Various stars experience such substantial variations from once every several years to once every several decades.

This shows that the interaction between the circumstellar disk and central star is active, and is accompanied by appreciable mass transfer through the circumstellar disk.

All this suggests that a typical, comparatively inactive T Tauri star should have a type I light curve. The other types of light curves can result from additional physical processes influencing the star, such as the accretion of matter from a circumstellar disk, eclipses by circumstellar matter, outbursts, effects associated with binarity, etc. This suggests that the main "stationary" object for all the light-curve types is the star itself, which probably has a magnetically active, spotted surface (e.g. Petrov et al., 1999).

Thus, the proposed classification scheme for T Tauri light curves is in reasonable consistency with current concepts concerning mechanisms for the variability of young stars. Note, however, that, bearing all these general features in mind, individual interpretation is needed for each particular observed T Tauri light curve.

References

Grankin K.N. et al.: 2007, *A&A,* **461**, 183.
Herbig G.H.: Adv. 1962, *A&A*, **1**, 47.
Herbst W. et al.: 1994, *AJ*, **108**, 1906.
Joy A.H.: 1945, *ApJ*, **102**, 168.
Parenago P.: 1954, *Publ. Shtern. Astron. Institute,* 25.
Petrov P.P. et al.: 1999, *A&A*, **341**, 553.
Pojmanski G.: 2002, *Acta Astronomica*, **52**,397.

HE I 5876 LINE STRUCTURE IN THE SPECTRA OF IL CEP A

N.Z.Ismailov, O.V.Khalilov, G.R.Bahaddinova

Shamakhy Astrophysical Observatory after named N.Tusi of ANAS
AZ 5626, Y.Mamedaliyev set., ShAO, Shamakhy, Azerbaijan, *ismailovn@yahoo.com*

ABSTRACT. We are presents the results of researches of the He l λ5876 Å (D_3) line in the spectrum of Herbig Be type star IL Cep A. This line represents the absorption structure which has a width on the level of the continuum about 15-18 Å, and a FWHM about 6-8 Å. It is shown that the line Hel λ5876 Å has a complex, multi-component structure. The average value of the radial velocities showed smooth variability, and the maximum value Vr achieved in 2009-2010. Large scatter in radial velocity was obtained in 2013 and 2014.

The equivalent width of the line also shows significant changes from year to year, and during the observation season. The total average value of this parameter remains constant for all observations. For all of the data, a mean value of the equivalent width of the absorption is equal 0.56±0.025 Å, and the standard deviation ±0.16 Å from the mean. The observed features in the line indicates that the field of origin this line has a complex structure and physical conditions.

Keywords: Pre-Main Sequence stars, spectral variability, helium D_3 line, IL Cep A.

1. Introduction

Herbig Ae/Be stars (HAeBes) are pre-main sequence (PMS) objects of intermediate mass approximately from 2 to 8 $M_\odot$ (Herbig, 1960; Finkenzeller & Mundt, 1984; Thé et al., 1994), spectral classes from B0 to F2 and types of luminosities IV-V. They are surrounded by dust/gas accretion disks. Disks of HAeBes have a complex spatial structure and contains an accretion regions and matter outflows in the form of a stellar/disk wind at higher latitudes.

HAeBe stars may be the precursors of young main sequence β-Pictoris and Vega-type stars. These latter systems are surrounded by circumstellar debris disks, which perhaps contain planetary bodies. This would imply that the environment around HAEBE stars represents an early phase in the formation of planets.

HAeBe stars are important astrophysical objects because they represent the late formative stages of intermediate mass stars. They are therefore significant for understanding general and specific phenomena involved in star formation. Moreover, HAeBe stars can help us to understand a number of perplexing properties of their main sequence (MS) descendants: in particular chemical peculiarities, very slow rotation, and magnetic fields, observed in individually or in combination in a significant fraction of MS A/B stars.

The star HD 216629 = IL Cep A (α_{2000}= $22^h53^m16^s$, δ_{2000}= +62°08″45′, $V{\sim}9.^m3$) is a member of young starformation region Cep OB3. At the distance 6.9″ (IL CepB=ADS 16341B) (Pirzkal et al., 1997) and even 0.44″ (Wheelwright et al., 2010) of the star it were separated two companions which are weaker in brightness to ΔB =3.5^m than the main component.

On the data of different authors the spectral type of IL CepA was determined as B2IV-V (Garmany, 1973), B3e (Finkenzeller, 1985), or as a components in visual binary B3 and B9 (Alecian et al., 2013). Radial velocities, equivalent widths and profiles of hydrogen lines are variable (see, e.g. Ismailov et al. 2013 and references there).

Hill (1967) firstly have determined the periodical variation in brightness of the star with the period 1.^{d}401, but later in the work (Hill et al., 1976) this periodicity was not confirmed.

One of consider question in the HAeBes spectrum is a structure and origin of the line D_3. This problem firstly in detail was studied by Böhm and Catala (1995). These authors showed that the line D_3 in HAeBes has mainly 2 type profiles: 1) clean absorption profiles and 2) absorption profiles which have blue shifted emission components. Some stars shows more complex structure. A question of the nature of different components in the line D_3 of young stars is object of discussion.

In this work we have presented results of long time researches the line D_3 structure in the spectrum of IL CepA.

2. Observations and results

The spectra were taken in 2006–2014 in the Cassegrain focus of the 2 m telescope of the Shamakhy Astrophysical Observatory of the Azerbaijan National Academy of Sciences. We used the UAGS-based spectrometer (Ismailov et al., 2013). A CCD detector is fixed in the focal plane of the camera. The 530×580 px CCD has a linear size of 9.5×13.9mm^2 and a pixel size of 18×24μm^2. The dispersion is equal to 10.5 Å/mm and about 6 Å/mm in the red and blue parts of the spectrum, respectively. The entire observed region of the spectrum can be covered by two frames. The spectrometer operates in 70–140 orders. The CCD window accommodates 28 and 50 orders in the red and blue parts of the spectrum, respectively. The normal spectrograph slit width determined by the CCD pixel size is 0.35 mm, which, given the effective Cassegrain focal length of 29 500 mm, corresponds to 2.

The spectrometer has a spectral resolution of R = 14 000, and a signal-to-noise ratio S/N=80–100 in the Hα region and S/N=20-40 in the HeI 5876 Å region. To control the stability of the system, the spectra of standard stars, the flat field image, and the comparison spectrum were taken every observing night at the beginning and end of the exposure of the object. Wavelength calibration was based on the spectrum of sunlight scattered in the Earth's atmosphere. We used the DECH20T program and its components developed at the Special Astrophysical Observatuum (Galazatdinov, 1992) to perform all the image reduction tasks and subsequent measurements of the spectra.

We used the lines of the Th-Ar lamp comparison spectrum to estimate the instrumental contour width, which we found to be 0.36 and 0.44 Å in the blue and red parts of the spectrum, respectively. The measured half widths of some lines exceed significantly the width of the instrumental profile: they are equal to 6–8 Å, 2–4 Å, and 4–7 Å, for Hα, Hβ, and D_3, respectively, and 0.8–1 Å and 1.5–2.0 Å for NaI D_1,D_2 and DIBs $\lambda\lambda$5780, 5798 Å, respectively.

We acquired a total of 50 pairs of spectrograms of the star for 2006-2014 years. Each pair consists of two identical spectra taken one after another. Three to four identical spectra of the star were taken on some nights.

The errors of the measured equivalent widths and intensities were equal to 5% and about 1%, respectively. The mean error of position measurements in the spectra of standard stars was 2–3 km/s. The measurement errors for the equivalent widths D_3 absorption sometimes exceed this limit because of the lower S/N ratio in the corresponding parts of the spectrum.

The line D_3 in the spectrum of IL CepA is represented as a wide absorption profile with width on the continuum at 15-18 Å and with a half width FWHM 6-8 Å. For this star in the work Tuairisg et al. (2000) was determined equivalent width of D_3 as 250 mÅ for absorption and 5 mÅ for emission components.

Because the line in our spectra has a complex structure the equivalent width we have determined by integration method for all boundary of contours. The radial velocity of the line was measured on the displacement of the line center at the half intensity level.

In the Figure 1 has shown a time variation of equivalent widths W_λ (up panel) and radial velocities Vr for the line D_3 (top panel).

As seen from the Figure 1 values of the equivalent width have some scatter from night to night but mean of this parameter is not so large changes during all time of observation. For all measurements mean value of equivalent width is equal 0.56 Å with dispersion ± 0.16 Å and with mean error of measurement ± 0.025 Å.

In 2013 radial velocities has shown variation from -12 to -32 km/s, this scatter bigger than in previous years. In 2014 the scatter in Vr is maximal, from -27 to +44 km/s. Moreover one can see smooth decrease of mean values Vr still 2010, then return to previous values. This character of variation in Vr of the line D_3 in more little scale is repeated variations of radial velocity of the emission component of Hα. This event also followed with unusual decreasing of equivalent width of Hα emission from -14 Å to -7 Å (Ismailov et al., 2013).
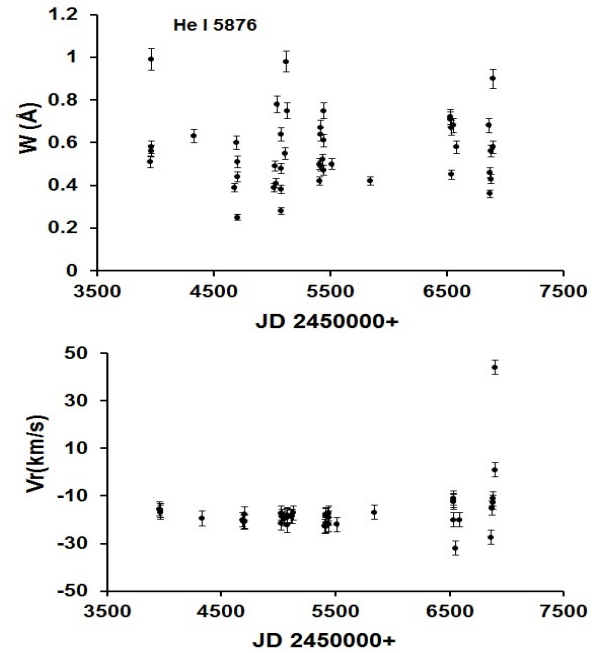

Figure 1: Time variation of equivalent widths W_λ (top panel) and radial velocities Vr (bottom) of the line D_3.

In Figure 2 are shown profiles of the line D_3 obtained in various nights. The profile shows complex structure which are consisting of some components. The structure shows variations for different nights. Moreover one can see some stable observable per night components. These components at 10-20 times stronger than the noise level, because we think that they are real components, possible consisting of emission components imposed to the weak absorption. Actually as has shown in Figure 2, the limit of noise intensity must be less or equal of the intensities of atmospheric H_2O lines placed near of lines D1, D2 NaI.

In detail a theory gives the following atomic transitions of the line He I 5876 Å (see, *http://physics.nist.gov/ PhysRefData/ASD/lines_form.html*) (Table 1).

Table 1: Atomic parameters of the line D_3.

Wavelength, Å	Transition level	log *gf*	relative intensity
5875.5987	2p ^{3}P^o– 3d ^{3}D	-1.511	
5875.6140	2p ^{3}P^o– 3d ^{3}D	0.480	5
5875.6148	2p ^{3}P^o– 3d ^{3}D		5
5875.6251	2p ^{3}P^o– 3d ^{3}D	- 0.338	5
5875.6404	2p ^{3}P^o– 3d ^{3}D	0.138	5
5875.9663	2p ^{3}P^o– 3d ^{3}D	-0.214	1

In columns were presented: wavelength in Å, levels of transition, log *gf*, where *g*-factor and *f*- the strength of oscillator, relative intensity. In our spectrum the lines 5875.61, 5875.62 and 5875.64 we have got as one unresolved line. The line 5875.966 is relative week than previous lines. Indeed as have seen in Figure 2 as a minimum we obtained 2-3 relative strong separated components in this line. But we count that these components may be results of variable emission which imposed to the wide absorption of this line.
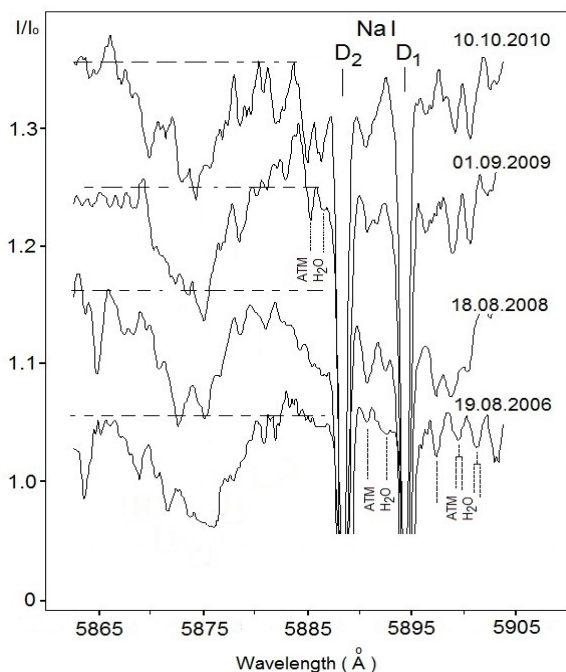
Figure 2: The structure of the line D_3 in the spectrum IL CepA.

In favor of our assumptions in Figure 3 have presented the profile of the line D_3 He I for spectrum of different HAeBes – AB Aur (Sp B9-A0V), HD 200775 (Sp B2-B3V) and supergiant 55 Cyg (Sp B3 Ia) which were observed in the same up mentioned equipment. As seen from the Figure 2 in spite of the fact that all these stars have in the spectrum the line D_3, the structure of the line as in IL Cep A is not detected. Moreover we have presented the profile of this line, for the spectrum IL Cep A obtained by Böhm and Catala (1995), where we see the same multicomponent structure in the line D_3. This comparison allows us to suppose that the complex structure in the line D3 may be connected of additional emission components in the line.

In the work by Tuairisg et al. (2000) authors tired determination of contribution of additional emission in this line for IL CepA. For it they are subtracted a theoretical profile of the line for corresponded spectral class from the observed profile of the line. As mentioned these authors, this procedure is followed many errors: to determination of real fundamental parameters of the star, influence of the noise, model calculations etc. Main of them on our opinion are connected with determinations of the real spectral class of IL Cep A, because as mentioned in Ismailov et al.(2013) the spectral class of the star were determined by different authors is different.
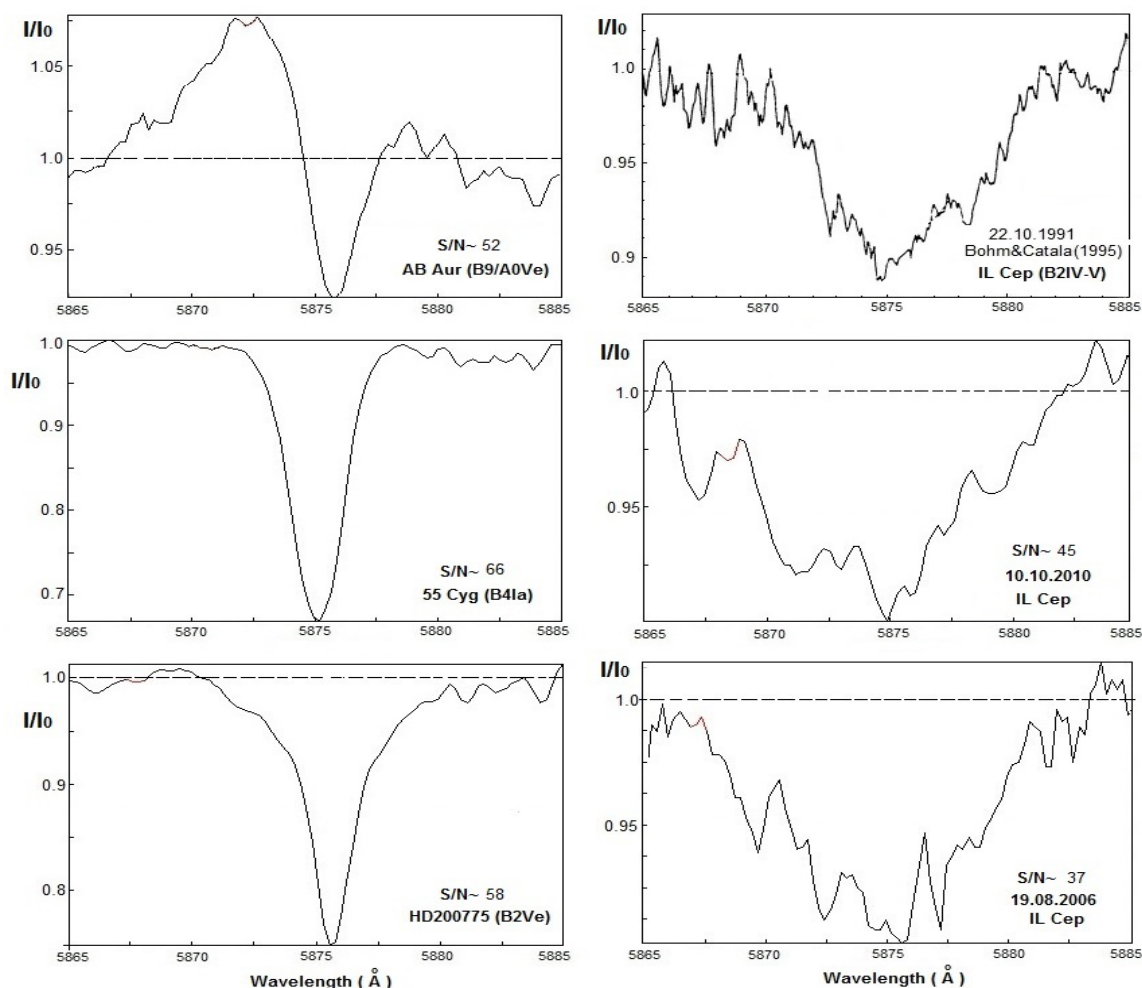

Figure 3: Profiles of the line HeI 5876 Å for different stars obtained in the same equipment: on the top right panel presented a profile of the line from the work by Bohm and Catala (995). For each panel S/N level have presented.

As a first step by using Mihalas (1964) theoretical profiles of the line HeI 5876 Å (for T_{eff} =20000 K and lg g=4.0) and taking into account a rotational velocity of IL Cep A as 180 km/s (Ismailov et al.2013, Melnikov et al. 1996) we have try to determine the contribution of emission component imposed to the helium absorption. In Figure 4a,b for example we have presented a residual profiles of the line for 2007 and 2009 obtained by dividing the observational profile to the theoretical with corresponding parameters. As seen from this figures in each case we have residual emission components. This fact as a minimum shows that the observational profile of the star perhaps is consisting of superposition of emission and absorption components.
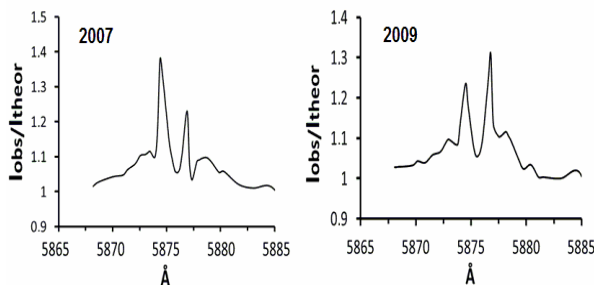

Figure 4: The residual structure obtained by dividing of the observational profile to the model.

3. Conclusions

Thus we have analyzed a structure of the D_3 line helium in the spectrum of HAeBes IL Cep A. We concluded that the line has complex multicomponent and variable structure. Some of components in the profile are real and connected with emission from the star envelope or disk. This line represents the absorption structure which has a width on the level of the continuum about 15-18 Å, and a FWHM about 6-8 Å. Although equivalent widths of the line demonstrated some scatter for different seasons of observation, the mean value of this parameter is not varied from year to year.

The radial velocity in the line D_3 shows the smooth variation with a minimum in 2010. This character of variation in Vr of the line D_3 in more little scale is repeated variations of radial velocity of the emission component of Hα. In 2013 and 2014 we have observed large scatter in radial velocities perhaps connected with activity in the circumstellar environment. A long time smooth variation in Vr perhaps occurred by dynamical motion in the binary system.

References

Alesian E. et al.: 2013, *MNRAS*, **429**, 1001A.
Böhm T., Catala C.: 1995, *A&A*, **301**, 155.
Finkenzeller U.: 1985, *A&A*, **151**, 340.
Finkenzeller U., Mundt R.: 1984, *A&AS*, 55, 109.
Galazutdinov G.A.: 1992, *Preprint of the Special Astro-physical Observatory*, No. 92.
Garmany C.D.: 1973, *AJ*, **78**, 185.
Harwey J.V., Tandberg-Hanssen E.: 1968, *SoPh.*, **3**, 316.
Herbig G.H.: 1960, *ApJS*, 4, 337.
Hill G. et al.: 1976, *Publ. Dom. Astrophys. Observ.*, **15**, 1.
Hill G.: 1967, *ApJSS.*, **14**, 263.
Ismailov N.Z. et al.: 2013, *Astrophys. Bull.*, **68**, 196.
Mel'nikov S.Yu. et al.: 1996, *Astron. Reports*, **40**, 350.
Mihalas D.M.: 1964, Pasadena, California, 220 p.
Pirzkal N. et al.: 1997, *ApJ*, **481**, 392.
Thé P.S. et al.: 1994, *A&AS*, **104**, 315.
Tuairisg S.O. et al.: 2000, *A&AS*, **142**, 225.
Wheelwright H.E. et al.: 2010, *MNRAS*, **401**, 1199.

SEASONAL VARIATIONS OF THE IONOSPHERE SCINTILLATIONS PARAMETERS OBTAINED FROM THE LONG OBSERVATIONS OF THE POWER COSMIC RADIO SOURCES AT THE DECAMETER WAVE RANGE

O. A. Lytvynenko, S. K. Panishko

Observatory URAN-4, Institute of Radio Astronomy NASU
Pushkinskaya str., 37, Odessa, 65125, Ukraine, spanishko@ukr.net

ABSTRACT. Observations of the four power cosmic radio sources were carried out on the radio telescope (RT) URAN-4 during 1987-1990 and 1998-2007 at the frequencies 20 and 25 MHz. Effects of ionosphere and in particular existence of intensity fluctuations on the cosmic radio sources records, or scintillations, are essential at the decameter wave range. Long series of the ionosphere scintillations parameters such as indices, periods and spectrum slopes were obtained after observation data proceeding. Behavior of the seasonal variations was investigated on this data. Obtained dependencies were compared with the indices of the solar and geomagnetic activity.

Keywords: radio sources: ionosphere scintillations, seasonal dependence

1. Introduction

Ionosphere scintillations are essential effect during observations in the decameter range of the radio waves. Long series of the ionosphere scintillations parameters such as indices, characteristic times (periods) and spectrum slopes of the signal from source might be obtained after processing of long standing measurements of discrete cosmic radio sources records. Previous investigations of the scintillation parameters time variations were showed an existence of the year cycle or seasonal-daily dependence in parameter's behavior (Kravetz et al., 2004; Panishko et al., 2008). This behavior is very variability on the small time intervals because intensity fluctuations (scintillations) are arises in such variable medium as ionosphere. Monthly meaning is the most optimum interval for studying of the scintillation parameter long time variations. The aim of this work is investigation of ionosphere scintillation parameter behavior on the base of the long measurement series.

2. Observations

The index, period and spectrum slope values of the ionosphere scintillations were calculated by processing of the four power radio source (3C144, 3C274, 3C405, 3C461) records, which were obtained on the radio telescope URAN-4 during 1987-1990 and 1998-2007 at the frequencies 20 and 25 MHz. Processing method was presented in the work (Derevyagin et al., 2005). Observations that carried out during 1987-1990 were

registered on the paper tape of recorder and processed by manual manner. The spectrum calculating do not carried out in this case therefore only scintillation index and period data are available. Time interval 1998-2007 was decided to 1998-2002 and 2003-2007 because the long data interruption was in the beginning 2003 on the technique reasons. The monthly mean values of studying parameters were obtained from initial data.

3. Results and their discussion

The ionosphere scintillation index data would considered in this work. Monthly mean values of scintillation indices *SI* for interval 1987-2007 at frequencies 20 and 25 MHz are plotted in the Fig. 1. The long time variations are remarkable in a behavior of the values *SI*, which corresponds previously observed seasonal-daily dependence. Others scintillation parameters – periods and spectrum slopes – are showed similar behavior but do not considered here because paper volume is limited.
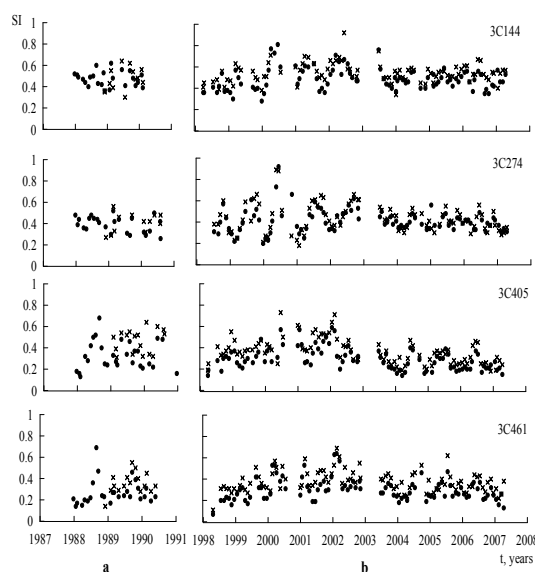

Figure 1: Monthly mean values of the ionosphere scintillation indices for 4-th radio sources: a – for time interval 1987-1990; b – for 1998-2007. Here and further crosses are marked values obtained at frequency 20 MHz, circles – at 25 MHz.
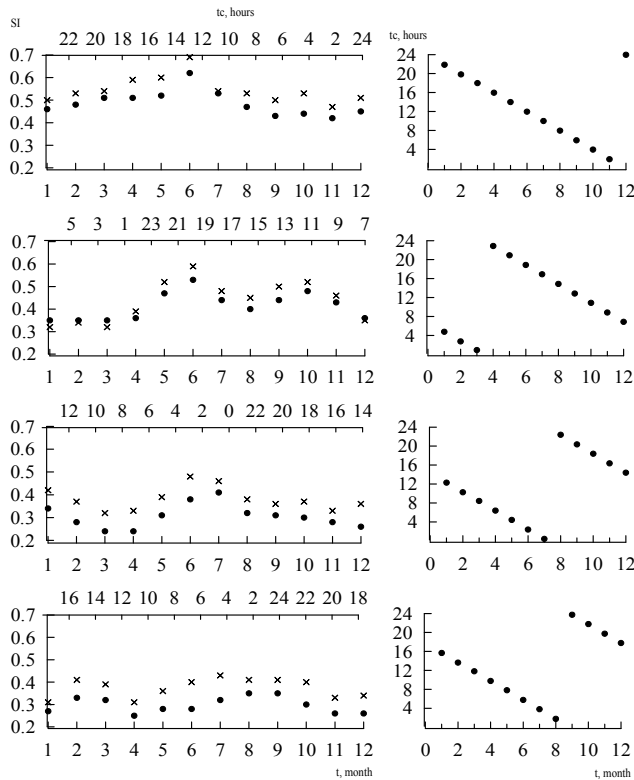
Figure 2: Scintillation indices for 4-th radio sources and 2-th frequencies meaning during month interval for all years observed. On the top axe are showed radio source culmination times for middle of the month. On the right: changing of the culmination time during year

Figure 3: Contour graphics of scintillation index dependence on month of year and radio source culmination time

Table 1: Correlation coefficients between data series at two frequencies

Years Source	1987-1990	1998-2002	2003-2007
3C144	0.84	0.77	0.99
3C274	0.51	0.69	0.53
3C405	0.40	0.79	0.73
3C461	0.34	0.87	0.71

It can be note that this is sufficient coincidence between scintillation index data on two frequencies. Corresponding values of the correlation coefficients are presented in Table 1. This result demonstrates similar conditions in which ionosphere scintillations arises at two frequencies.

The values meaning during the month intervals for all scintillation index data considered are presented in the Fig. 2. It can be seen that behavior of the index *SI* is similar at two frequencies but different for radio sources. If compared graphics in the Fig. 2 with contour maps in the Fig. 3 we can see that scintillation index behavior depends on that how culmination time of the radio sources change during the year. In general it may be noted that scintillation index maximum values reached in June-August and October and minimum values – in March-April, August-September and November.
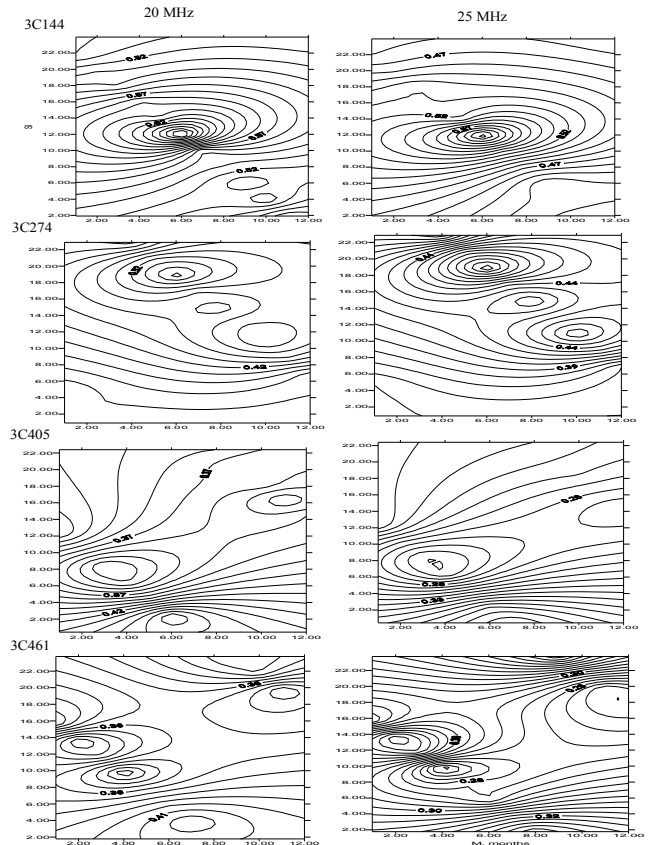
Besides year cycle scintillation indices are showed long time trend which caused by influence of the solar activity cycle. For second and third observation time intervals the low frequency part was distinguished by fitting of the second order polynomial function. Such procedure was fulfilled for the monthly mean of solar and geomagnetic indices – number of solar spots, radio flux at the frequency 10 cm and Ap-index. In result we obtained those values of the correlation indices between low frequency part of scintillation indices dependence and solar and geomagnetic index behavior change in following limits with:

a) number of solar spots: 0.38-0.99;
b) radio flux at the frequency 10 cm: 0.39-0.99;
c) geomagnetic index Ap: 0.46-0.96.

It's sufficiently high means and confirmed the connection with solar activity.

4. Conclusions

Investigations of the ionosphere scintillation index seasonal dependence were carried out for 4-th power cosmic radio sources at two frequencies in the decameter wave range. Following results were obtained.

Previously known seasonal-daily dependence in behavior of the scintillation index monthly mean of the 4-th power discrete cosmic radio sources at the

frequencies 20 and 25 MHz was confirmed for a long time interval of data.

It was established that scintillation index series at the two frequencies of the decameter range of radio waves have sufficiently good correlation.

It was investigated that the type of changing of scintillation index behavior during season and daily depended on that how culmination time of the radio source change during year.

Low frequency part of ionosphere index dependence has sufficiently high values of the correlation coefficients with solar number spots, radio flux at the frequency 10 cm and geomagnetic Ap-index.

References

Kravetz R.O. et al: 2004, *Odessa Astron. Publ.*, **17**, 42.
Panishko S.K. et al.: 2008, *Radiofizika i Radioastronomiya*, **13**, S130 (in russian).
Derevyagin V.G. et al.: 2005, *Astron. and Astrophys. Trans.*, **91**, 421.

LUMINOSITY-LINEAR SIZE RELATION FOR GALAXIES AND QUASARS WITH STEEP RADIO SPECTRUM

A.P.Miroshnichenko

Institute of Radio Astronomy, NAS of Ukraine
4, Chervonopraporna Str., 61002, Kharkiv, Ukraine
mir@rian.kharkov.ua

ABSTRACT. Our data for sources with steep radio spectrum, detected with radio telescope UTR-2 at the decametre band give evidence on the great luminosities, linear sizes, characteristic ages of these objects. In connection with such peculiarities, we examine the luminosity-linear size relation of galaxies and quasars with steep radio spectrum at the decametre band. It turned out, that this relation has similar trends for considered radio sources with linear steep spectrum and break steep spectrum. Also we presented the luminosity ratio-linear size relation at different frequency ranges. We discuss the obtained evolution relations for galaxies and quasars with steep low-frequency radio spectrum.

Keywords: Galaxies: steep radio spectrum – Galaxies: luminosity – Quasars: steep radio spectrum – Quasars: luminosity

1. Introduction

For the purpose of further study of the peculiar class of objects – galaxies and quasars with low-frequency steep radio spectrum (the spectral index values are larger 1), we consider the relation of their radio luminosity and linear size. This relation, as pointed out Shklovskii (1963), may contain the information on the source's evolution. A number of authors (Kapahi, 1989; Gopal-Krishna & Kulkarni, 1992; Neeser et al 1995; Singal, 1996; Luo & Sadler, 2010) have studied the dependence of linear size on luminosity for radio galaxies and quasars, but there is no the single opinion. For instance, Kapahi (1989) obtained for powerful radio galaxies an increase of source's sizes at large luminosities, while Luo & Sadler (2010) established the same trend only for sources with low radio luminosity. Note, that majority of the authors have used samples of objects irrespective of range of the spectral indices. It is known, spectral indices of non-thermal radio spectra may be connected with acceleration mechanisms of relativistic particles and evolution of sources. The detailed study of the identified radio sources with steep spectra at the decametre band (Miroshnichenko, 2010, 2012a, 2012b, 2013, 2014, 2015) shows, that these radio sources have interesting properties. In particular, these objects have great luminosity ($L_{25} \sim 10^{28}$ W/Hz ster), great characteristic age (10^8 years), giant radio structure (~ 1 Mpc). It is noteworthy that the obtained energy ratio for steep-spectrum sources (Miroshnichenko, 2014) testifies that the energy of relativistic particles prevails over the energy of magnetic field in the galaxies and quasars with steep radio spectra.

2. Luminosity – linear size relation for powerful giant sources

From the UTR-2 catalogue (Braude et al., 1978, 1979, 1981a, 1981b, 2003) we have formed sample of radio sources with steep spectrum including objects with linear steep spectrum (S-type) and spectrum with low-frequency steepness after a break (C+ type). Within the declination ranges from -13 to +20 degrees and from 30 to 40 degrees of the UTR-2 catalogue we have identified 78 galaxies and 55 quasars with linear steep spectrum (S-type) and 52 galaxies and 36 quasars with break steep spectrum (C+type) (with flux density at 25 MHz $S_{25} > 10$ Jy and spectral index larger 1). We use the NED database (http://nedwww.ipac.caltech.edu) for the high-frequency and optical identifications. Estimates of the angular sizes of examined sources we have derived from the corresponding radio images of the NVVS survey (at frequency 1400 MHz), presented at NED database. We suppose, that angular sizes from NVSS are close to angular sizes of corresponding sources at low frequencies. Calculations of the physical parameters of considered radio sources are carried out at cosmological parameters $\Omega_m = 0.27$, $\Omega_\lambda = 0.73$, $H_0 = 71$ km/s Mpc. Table 1 presents the characteristic values of derived parameters of sample objects: $<z>$ - is the mean value of the redshifts of considered class of objects; z_{median} – is the median value of the redshifts; $<L_{25}>$ – is the mean value of the monochromatic luminosities at the frequency 25 MHz; $<R>$ – is the mean value of the linear sizes of objects.

Table 1. Parameters of the sample sources

Objects	$<z>$	z_{median}	$<L_{25>(W/Hzsr)}$	$<R>(cm)$
G_S	0.697 (+-0.105)	0.364	3.27(+-1.18) 10^{28}	6.09(+-0.64) 10^{24}
G_{C+}	0.308 (+-0.076)	0.182	8.14(+-5.73) 10^{27}	3.50(+-0.52) 10^{24}
Q_S	1.029 (+-0.070)	0.944	5.17(+-1.35) 10^{28}	9.75(+-0.53) 10^{24}
Q_{C+}	0.950 (+-0.092)	0.857	4.78(+-1.73) 10^{28}	8.73(+-0.75) 10^{24}

As one can see from the Table 1, galaxies and quasars with steep low-frequency spectrum are characterized by

great radio luminosity at the decameter band and the giant linear size. We examine relationship L_{25} (R) of radio luminosity at 25 MHz and linear size for each class of objects in our sample, that is, in 4 subsamples, which are: galaxies with linear steep spectrum (G_S), galaxies with break steep spectrum (G_{C+}), quasars with linear steep spectrum (Q_S), quasars with break steep spectrum (Q_{C+}). At this, the relation L_{25} (R) is considered at different ranges of redshift z relatively to median values z_{median} in given subsamples (see Figure 1 – Figure 6).
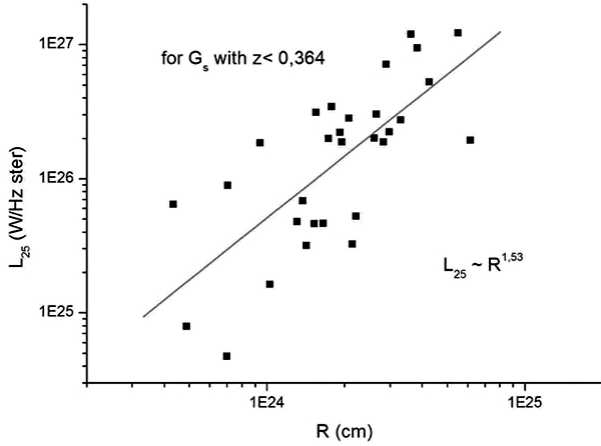

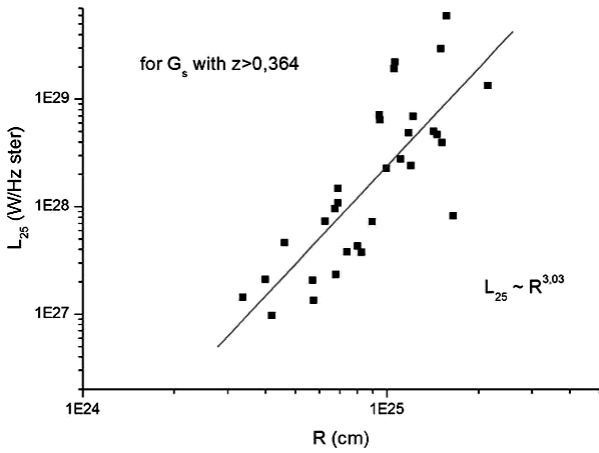Figure 1: Luminosity at 25 MHz versus linear size for G_S at $z < z_{median}$

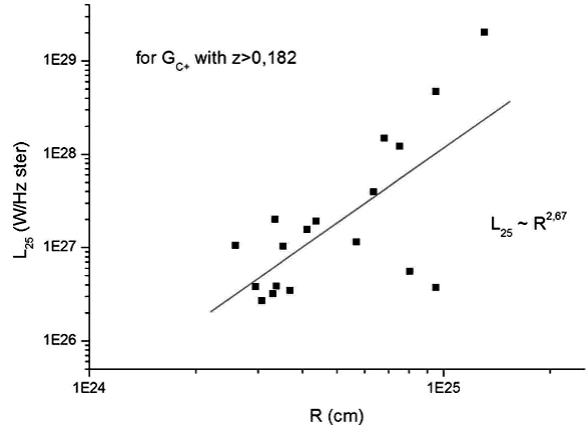Figure 2: Luminosity at 25 MHz versus linear size for G_S at $z > z_{median}$

Figure 3: Luminosity at 25 MHz versus linear size for G_{C+} at $z > z_{median}$

Figure 4: Luminosity at 25 MHz versus linear size for Q_S at $z < z_{median}$

Figure 5: Luminosity at 25 MHz versus linear size for Q_S at $z > z_{median}$

Figure 6: Luminosity at 25 MHz versus linear size for Q_{C+} at $z < z_{median}$

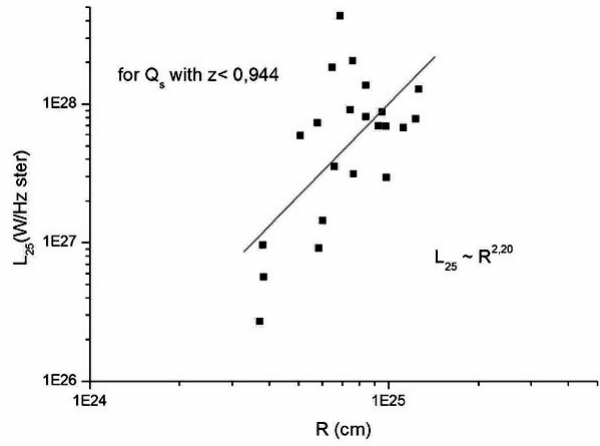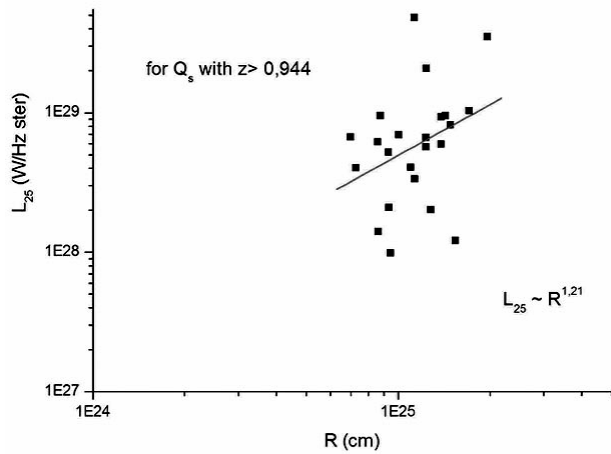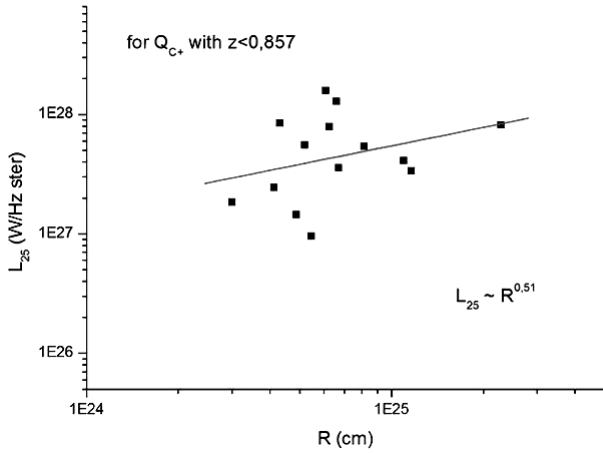The derived relations L_{25} (R) have the power trend (see Figures 1 – 6 and Table 2).

Table 2. Relations L_{25} (R) in 4 subsamples (G_S, G_{C+}, Q_S, Q_{C+}) at redshift ranges z, less z_{median}, and larger z_{median}

Objects /and their z_{median}	L_{25} (R) at $z < z_{median}$	L_{25} (R) at $z > z_{median}$
G_S /0.364	$L_{25} \sim R^{1.53 \, (+-0.27)}$	$L_{25} \sim R^{3.03(+-0.43)}$
G_{C+} /0.182	$L_{25} \sim R^{0.98 \, (+-0.40)}$	$L_{25} \sim R^{2.67(+-0.70)}$
Q_S /0.944	$L_{25} \sim R^{2.20 \, (+-0.60)}$	$L_{25} \sim R^{1.21(+-0.75)}$
Q_{C+} /0.857	$L_{25} \sim R^{0.51 \, (+-0.44)}$	$L_{25} \sim R^{1.57(+-0.98)}$

It is interesting that the ratio of corresponding luminosities at decameter and optical bands (L_{25} / L_{opt}) for sample objects displays the similar correlation with linear size of sources (see Figure 7, Figure 8).
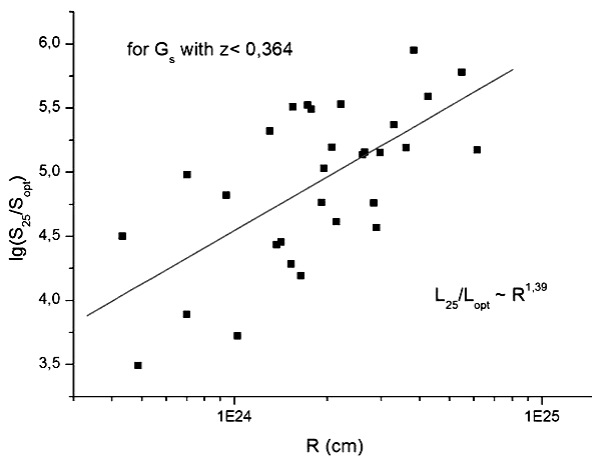

Figure 7: Ratio of luminosities at decametre and optical bands versus linear size for G_S at $z < z_{median}$

We can consider the ratio of decametre and optical luminosities of source as the ratio of emission of extended component and central component of source. As it follows from Figure 7 and Figure 8, the relative contribution of the decametre emission in steep-spectrum sources increases for more extended objects.
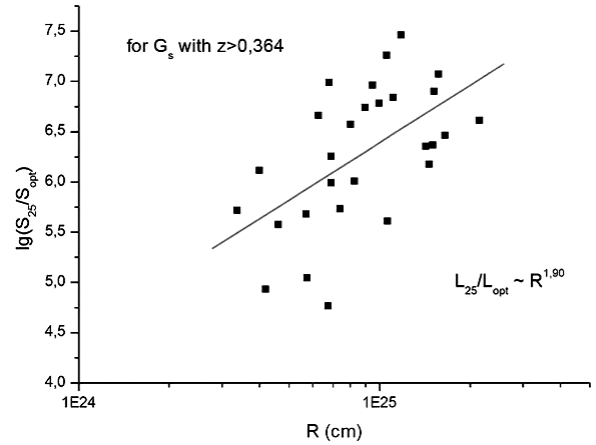

Figure 8: Ratio of luminosities at decametre and optical bands versus linear size for G_S at $z > z_{median}$

Also, we study the relation L_{25} (R) at the same range of redshifts: $z = 0 – 0.5$ for each subsample of objects. It turned out that obtained relations have the power shape:

for G_S : $L_{25} \sim R^{1.93 \, (+-0.22)}$
for G_{C+} : $L_{25} \sim R^{1.81 \, (+-0.25)}$
for Q_S : $L_{25} \sim R^{1.80 \, (+-1.06)}$
for Q_{C+} : $L_{25} \sim R^{0.25 \, (+-0.94)}$

So, galaxies and quasars with steep spectrum and giant radio structure reveal the positive correlation of their radio luminosity and linear size. Within the limits of statistical errors the derived power indices of the relation L_{25} (R) are enough close in values for galaxies and quasars of our sample. The noticeable disperse at the each found relation L_{25} (R) for sources with steep radio spectrum may be caused by cosmological evolution of linear size, that is, the relation of linear size and redshift, R (z). To exclude the influence of itself cosmological model used at calculation of source's physical parameters, we search for the relation R (z) only at given bins of luminosity L_{25} (at bin value Δ lg L_{25} = 1). For example, at the luminosity bin L_{25} = $10^{28} – 10^{29}$ (W/Hz ster) the derived relation R (z) shows power trend in 4 subsamples:

for G_S : $R \sim (1+z)^{0.74 \, (+-0.38)}$
for G_{C+} : $R \sim (1+z)^{0.97 \, (+-0.27)}$
for Q_S : $R \sim (1+z)^{0.83 \, (+-0.52)}$
for Q_{C+} : $R \sim (1+z)^{1.87 \, (+-0.42)}$.

One can note the more considerable evolution of the linear size of quasars with break steep radio spectrum (C+type). This corresponds to great characteristic age of these objects. According to our previous estimates of characteristic age of sources with steep radio spectrum (Miroshnichenko, 2013) the age of galaxies and quasars with spectrum of C+type is $\sim 10^8$ years, and near one order is larger than the characteristic age of sources with steep spectrum of S – type.

3. Conclusion

Empirical relations of luminosity and linear size have been derived for samples of powerful galaxies and quasars with low-frequency steep spectrum and giant radio structure.

Within the limits of statistical errors the power shape of the relation of luminosity and linear size is, practically, the same for galaxies and quasars with steep spectrum.

The cosmological evolution of linear size of galaxies and quasars with steep radio spectrum have been revealed, at that quasars with spectrum C+ show the more considerable evolution.

The found relation of decametre luminosity and linear size points out on the huge power of the "central engine" of sources with steep radio spectrum, which provides for rejection of jets to giant distances (~ Mpc).

References

Shklovskii I.S.: 1963, *SvA*, **6**, 465.
Kapahi V.: 1989, *AJ*, **97**, 1.
Gopal-Krishna & Kulkarni V.: 1992, *A&A*, **257**, 11.
Neeser M. et al.: 1995, *ApJ*, **451**, 76.

Singal A.: 1996,in *Extragalactic Radio Sources*, Dordrecht, 563.
Luo Q. & Sadler E.: 2010, *e-print*, arxiv: 1003.0667.
Miroshnichenko A.: 2010, in *Astrophysics and Cosmology after Gamow,* New York, AIPC, **80**, 335.
Miroshnichenko A.: 2012a, *Radio Physics and Radio Astronomy,* **3**, 215.
Miroshnichenko A.: 2012b, *Odessa Astron. Publ.,* **25**, 197.
Miroshnichenko A.: 2013, *Odessa Astron. Publ.,* **26/2**, 248.
Miroshnichenko A.:, 2014, in *Multiwavelength AGN Surveys and Studies*, Cambridge, 96.
Miroshnichenko A.: 2015, *e-print*, arxiv: 1505.01870.
Braude S.et al.: 1978, *Astrophys. Space Sci.,* **54**, 37.
Braude S.et al.: 1979, *Astrophys. Space Sci.,* **64**, 73.
Braude S.et al.: 1981a, *Astrophys. Space Sci.,* **74**, 409.
Braude S.et al.: 1981b, *Astrophys. Space Sci.,* **76**, 279.
Braude S.et al.: 2003, *Kinem. Phys. Celest. Bod.,* **19**, 291.

THE DAILY 110 MHZ SKY SURVEY (BSA FIAN):
ON-LINE DATABASE, SCIENCE AIMS AND FIRST RESULTS
OF DATA PROCESSING

V.A.Samodurov [1,2], A.E.Rodin [1,2], M.A.Kitaeva [1], E.A.Isaev [1,2], D.V.Dumsky [1],
D.D.Churakov [3], M.O.Manzyuk [4]

[1] Pushchino Radio Astronomy Observatory ASC LPI, Pushchino, Russia, *sam@prao.ru*
[2] National research university Higher school of economics, Moscow, Russia
[3] TSNIIMASH, Moscow, Russia
[4] Internet portal BOINC.Ru

ABSTRACT. From 2012 on radio telescope BSA FIAN multi beams diagram was started. It capable at July 2014 daily observing by 96 beams in declination -8 .. 42 degrees in the frequency band 109-111.5 MHz. The number of frequency bands are from 6 to 32, the time constant are from 0.1 to 0.0125 sec. In receiving mode with 32 band (plus one common band) with a time constant of 12.5 ms (80 times per second) respectively produced 33x96x80 four byte real and so daily we produced 87.5 Gbt (yearly to 32 Tbt). These data are enormous opportunities for both short and long-term monitoring of various classes of radio sources (including radio transients) and for space weather and the Earth's ionosphere monitoring, for search for different classes of radio sources, etc. The base aims of our work are:

a) to obtain new scientific data on different classes of discrete radio sources, the construction of physical models and their evolution - obtained on the basis of the clock continuous digital sky radio monitoring at frequency 109-111.5 MHz and cross-analysis of data from third-party reviews on other frequencies;

c) launch the streaming data on various types of high-performance computing systems, including to create a public system of distributed computing for thousands of users on the basis of BOINC technology. The BOINC client for astronomical data from the monitoring survey of the big part of entire sky almost have not analogies.

We have some first science results (new pulsars, and some new type of radiosources).

Keywords: Stars: abundances – Galaxy: abundances – stars: late-type

1. Observations

In 2012 the multi-beam feed array has become operational on the BSA FIAN radio telescope (Oreshko et al, 2012). As of July 2015 it is capable of 24-hour observation using 96 beams in declination of -8 to +42 degrees in the 109-111.5 MHz frequency band.

The number of frequency bands range from 6 (417 kHz per band as the "wide observational mode" or "light" mode) to 32 (78 kHz per band as the "narrow observational mode" or "heavy" mode) while the time constant ranges from 0.1 sec ("wide observational mode") to 12.5 ms ("narrow observational mode"). Such type of continu-

ous daily survey of the major observable part of the sky is not yet done by any observatories worldwide. Observations have already been carried out for more than 2.5 years, with a typical daily data production of 2.3 GB (gigabytes) in wide observational mode, equating to a total of 0.8 TB (terabyte) of data per year. Respectively, in narrow observational mode the data produced amounts to 87.5 GB daily, or 32 TB yearly.

It is now possible to record data in both modes at the same time. The narrow observational mode will be used in the near future for the purpose of searching for radio transients of different types (for example, pulsars). At the end of October 2015 we accumulated over 16 months of observations "heavy" mode (total volume of about 41.6 TB) and more than 3 years for "light" mode (total volume of about 3 TB).
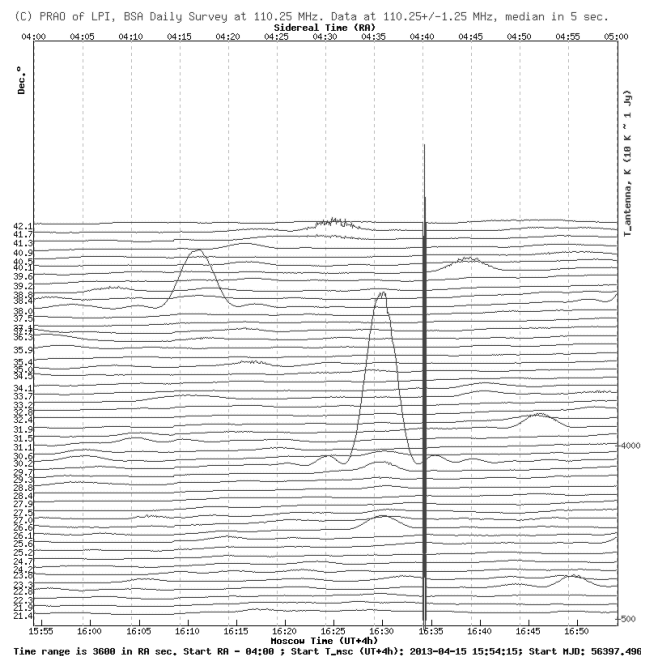

Figure 1: The sample of calibrated data from the multi beams diagram BSA at 15 April 2013. It showed the calibration signals (at RA = 4 h 40 m) of galaxy background with the some radio sources on it. The some sources (for example is upper sources) are showed phenomenon of flicker produced by interstellar medium scintillations from small sources with scales nearly fraction of arc second.

2. Database and data processing

A specialized database needs to be constructed to facilitate the large amount of observational data. In the period between 7 July 2012 and 20 October 2013 an experimental database collected more than 8 million calculated 5-second sample data from each beam for more than 27 parameters. The observational data parameters are maximal, minimal, median, average, dispersion etc. for 5-second periods of time in different frequency bands. Using this data close to one million images has been built. The figure 1 present example median data on hourly scale.

By the end of 2014 work will be completed on the online database, which will be publically available on http://astro.prao.ru/. This database will enable users, both local and remote, to use different ways to processing the observation data. The total size of the database is over than 200 GB.

We should highlight the fact that storing the compressed data in SQL database formats allows us to use the power of selection, sorting, matching, filtering and initial processing of data by using standard SQL commands. This will greatly simplify the interaction and the comparative analysis of the data for different sorts of data and their cross-temporal analysis, averaging etc. These data are enormous opportunities for both short and long-term monitoring of various classes of radio sources (including radio transients) and for space weather and the Earth's ionosphere monitoring, for search for different classes of radio sources, etc.

One of our goals is to launch data streaming processes on various types of high-performance computing systems, including creating a public system of distributed computing for thousands of users on the basis of BOINC technology. The BOINC client for astronomical data from the monitoring surveys of large parts of the entire sky almost has no analogies.

Preliminary estimates show that we may reach of data processing speeds practically bordering on "on-line" mode (with a time lag of no more than 2-3 hours following the observations). All data, including the original observations and the results of data processing for the purpose of various scientific objectives will be continuously displayed on the PRAO of LPI website. The data will be displayed in graphical form for external public users, while the project participants will also be able to access the data in its original digital form.

For mutual benefit it is possible to also facilitate for this database to include additional low-frequency (10-25 MHz) observation data from the Ukrainian UTR radio telescope.

3. The scientific goals

This monitoring system allows a potential to solve a tremendously wide range of classes of problems, not only fundamental scientific ones, but also challenges within applied sciences. The proposed project allows to continuously monitor celestial radio sources in most parts of the sky on time scales from milliseconds to years.

The following is a list of our primary goals:

1) Monitoring of the ionosphere state and its fluctuations (with a characteristic time scale of tens of seconds).

2) Analysis of meteor tracks in the higher layers of the Earth's atmosphere.

3) Monitoring of active phenomena on the Sun such as sporadic outbursts with the time scales from seconds to hours as well as the state of the near-solar plasma. This is a broad field of research on near-solar source flicker interplanetary plasma. This solar behavior will be monitored and its most common parameters will be displayed in graphical form on the PRAO of LPI website.

4) Radio monitoring of transient (flare) phenomena in the solar system such as ionospheric and storm phenomena of the giant planets, tracking of radio transient phenomena on the Moon and other radio phenomena in the solar system.

5) Monitoring of transient phenomena in our Galaxy. This covers a wide class of scientific problems, from studies of outbreaks of radio emission from cataclysmic variables to search for candidates in exoplanets around alien stars. Not all of them can be implemented on our radio telescope, however some of these events are available to us.

6) Monitoring of flux density of extragalactic radio sources. For this purpose we are able to perform daily monitoring of about 400-500 radio sources outside of 15-degree declination from the plane of our Galaxy.

7) Monitoring of extragalactic transient phenomena. The most interesting problem is searching for fast radio transient events in other galaxies (on the scale of a few milliseconds). According to several studies such radio transients have been discovered in the decimeter wavelength range in the last few years. Theorists associate these transient events with the possible merges of neutron stars. Phenomena of this magnitude emit great amounts of energy, the levels of which are high enough to be detected by our telescope even from galaxies as distant from us as hundreds of Mpc. This problem is currently a very popular topic for Astrophysics.

Ultimately, the multi-beam observations of the BSA of LPI telescope will take advantage of the wide-field survey capabilities to enable the discovery and investigation of variable and transient phenomena from the intra- to the extra- galactical, including flare stars, intermittent pulsars, X-ray binaries, magnetars, extreme scattering events, interstellar scintillation, radio supernovae and orphan afterglows of gamma-ray bursts. In addition, it will allow us to probe unexplored regions of parameter space where new classes of transient sources may be detected.

4. The first scientific results

We have today from base data processing of the some first science results. It is the first results for search of the new pulsars and search results of the other objects.

It is best test of our data is the pulsars search. The best solving of this problem on our data can be processing by a on supercomputers computing or a by BOINC distributed computing (look on http://boinc.berkeley.edu/).

The example of the last way is the Einstein@Home project in the decimeter band of radio wave for the data from Arecibo radio telescope (Cordes, J.M. et al: 2006) and from Parkes Observatory data (Knispel et al , 2013). The project found in the observatory data more than 50 new pulsars at a frequency of 1440 MHz.
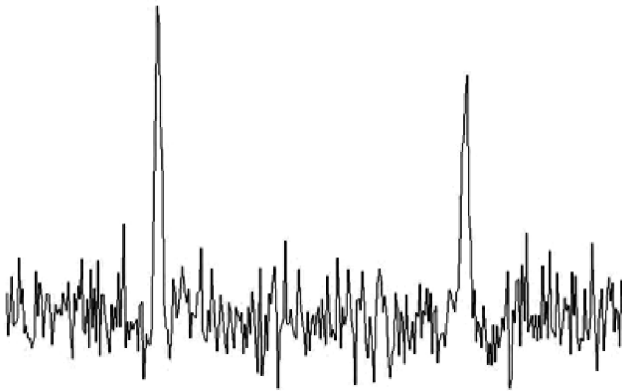
Figure 2: The result of search for new pulsar PSR $\alpha_{2000}=09^h28^m00^s\pm30^s$; $\delta_{2000}=+30°37'\pm20'$ with period P=2.0919s and DM=22-24 (from S.A.Tulbashev, V.S.Tulbashev, 2015). It is showed 2 pulsar periods.

BSA of LPI is one of the best in the world in antennas sensitivity parameter. Really, BSA effective area of approximately 30,000 square meters, which is about the same order as that in Arecibo and significantly more than Parkes radio telescopes. The pulsars is brighter by order on our frequency 110 MHz in additional. So although our frequency band is less (2.5 MHz against the tens of megahertz in Parkes and Arecibo), we may hope discover of some new pulsars in our data.

We began in April 2015 pulsars search in the standard regime by single personal computers as part of the work data testing. We have been using two searches methodic.

First method is classical folding – that is testing different periods and dispersion delay for pulsar candidate. Four new pulsar was already discovered by this work (S.A. Tulbashev, V.S. Tulbashev, 2015).

On the figure 2 is showed the result of searching for one from new pulsars that found by folding method (S.A. Tulbashev, V.S. Tulbashev: 2015).

The second method is search for new periodic objects by using spectral analysis. We dividing observation time in each beam scans on data segments that contain 2048 points (i.e., 2 in power 11, for to using of classical Fast Fourier Transform algorithms). So for the "small" mode of observation with a time constant of 0.1 seconds is provided time interval data equally 205 seconds. So we have near beam width BSA temporal scale (at the half power) that has about 5-6 minutes. Thus the range of 205 seconds is about twice less than the actual exposure time of sources. But this method allows summarizing the observations data from day to day. In result we will can find hundreds possible pre-candidates pulsar list with roughly defined periods $\pm0.0005^s$ by preprocessing FFT spectral analysis over all the sky. This big list of pre-candidates will be processing at next stage by BOINC computing. In result we hope found some very weak pulsar computing after preprocessing by FFT spectral analysis plus BOINC computing.

On the figure 3 is showed the result of checking data for this pulsar by FFT spectral analysis for sum all 3 year data (2012-2015) in observational "light" mode (with 0.1 sec time constant). We may look that both methods work very satisfactorily.
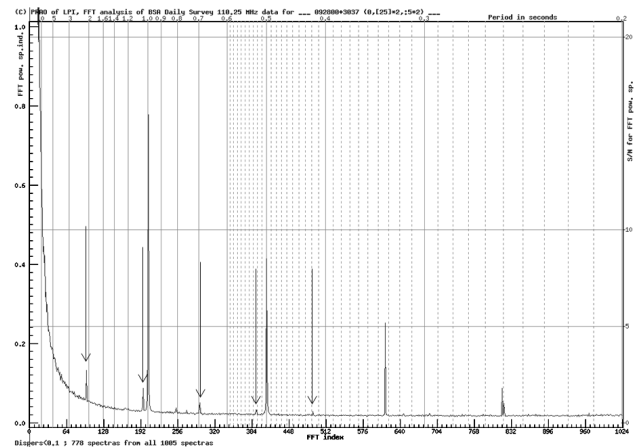

Figure 3: The result of testing for new pulsar PSR from figure 2 by FFT spectral analysis on 2012-2015 year data. The arrows marked 5 harmonics of the period P =2.0919 s. We may look also 4 harmonics of the period P=1.000 s that unfortunately produced by interferences from local GPS time receiver.

There are other scientific problems (sometimes quite unexpected nature) that can be solved with the help of your data. So, as an example of practical problems that proposed by one of the authors is search radar echoes from satellites that produce by ILS in airport near Moscow. An instrument landing system (ILS) is a ground-based instrument approach system that provides precision lateral and vertical guidance to an aircraft approaching and landing on a runway, using a combination of radio signals. ILS carrier frequencies range between 108.10 MHz and 111.95 MHz (with the 100 kHz first decimal digit always odd, so 108.10, 108.15, 108.30, etc., and are not used for any other purpose).

We not look (to our luck) direct radiation from ILS but we may look its echoes from Earth satellites. We really find reflections from the International Space Station in the target multi-beam diagram of BSA.

We did analysis of the 2 month statistics of detecting reflected radar signals indicated airfield complexes from the International Space Station. It is showed that in September-October 2013 there were 85 events across the track of the ISS (at a distance of 500-800 km away from the observer) target through diagram BSA. This 35-40 are reliably identified as short bursts of radio flux equally 10-20 Jy. Figure 4 shows one from these cases, where the ISS passing through BSA multi-beam diagram (which are directed along the South-North line). This work demonstrates that found radio transients in our survey data can be, unfortunately, also be produce manmade.

The figure 4 is showed that satellites track on the data is very symmetrical. But we also finding transient phenomena second timescale in non-symmetrical form and with traces of the influence of the dispersion delays. We will preparing in future some statistical work for this phenomena.
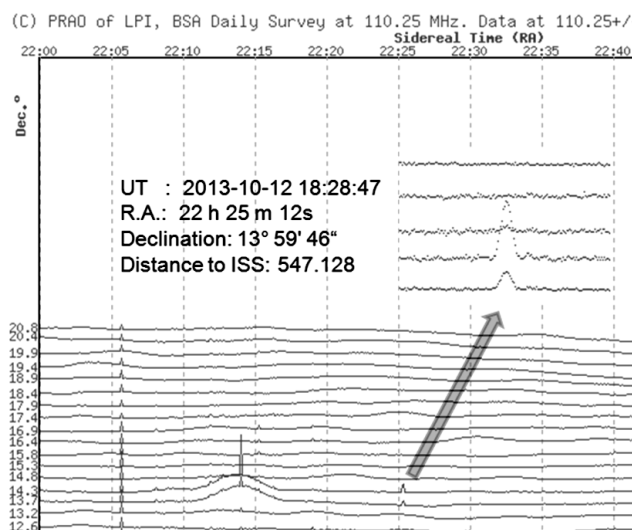
Figure 4: The result of ISS passing through BSA multi-beam diagram at 2013-10-12 in 18:28:47 UT. We may look that ISS at distance 547.1 km passing through diagram about 1.6 sec and has very symmetrical form.

5. Future prospects

This BSA monitoring system allows a potential to solve a tremendously wide range of classes of problems. The proposed project allows to continuously monitor of celestial radio sources in most parts of the sky on time scales from milliseconds to years. We hope produce thus regime of processing that all the work of patrol and processing possible transient phenomena, also as monitoring of known radio sources, searching for new sources and so on will be conducted in automatic mode.

The observational data will be automatically preprocessing and locating in total data base. At next stage we will find from this data base of some interesting goal for scheduled and will start processing on BOINC-server by method of distributed computing.

The part of the work will are produced from the known coordinates of some type of sources (for example the giant planets of the solar system, transients associated with cataclysmic variables, etc.).

Other part of sky targets will be produced by third-party information sources. It is in first different data base for example gamma-ray bursts data base and so on.

In our data reduction can be also included other long wave radio survey for cross testing. For example is the most low-frequency survey observations in word from the Ukrainian radio telescope UTR, also as Netherlands radio interferometric system LOFAR and so on.

References

Cordes J. M. et al: 2006, *AJ*, **637**, Issue 1, 446.
Knispel B. et al: 2013, *AJ*, **774**, Issue **2**, article id. 93.
Oreshko V.V. et al : 2012, *Transactions of the Institute of Applied Astronomy* (Russia), **24**, 80.
Tulbashev S.A., Tulbashev V.S.: 2015, *Astron. Tsirkular*, **1624**.

HIGH-FREQUENCY CUTOFF IN TYPE III BURSTS

A.A.Stanislavsky[1,2], A.A.Konovalenko[1], Ya.S.Volvach[1], A.A.Koval[1]

[1] Institute of Radio Astronomy, Kharkiv, Ukraine, *astex@ukr.net*
[2] V.N. Karazin Kharkiv National University, Kharkiv, Ukraine

ABSTRACT. In this article we report about a group of solar bursts with high-frequency cutoff, observed on 19 August of 2012 near 8:23 UT, simultaneously by three different radio telescopes: the Ukrainian decameter radio telescope (8-33 MHz), the French Nançay Decametric Array (10-70 MHz) and the Italian San Vito Solar Observatory of RSTN (25-180 MHz). Morphologically the bursts are very similar to the type III bursts. The solar activity is connected with the emergency of a new group of solar spots on the far side of the Sun with respect to observers on Earth. The solar bursts accompany many moderate flares over eastern limb. The refraction of the behind-limb radio bursts towards the Earth is favorable, if CMEs generate low-density cavities in solar corona.

Keywords: Sun: radio emission – bursts: UTR-2 radio telescope

1. Introduction

Sporadic radio emission of the Sun is observed in a wide range of wavelengths, from millimeters to kilometers. The radio waves emerge from different heights (layers) of the solar atmosphere: radiation of millimeter range is emitted by the lower chromosphere, cm-waves are produced by the middle and upper chromosphere, decimeters originate from the transition region, meters come from the lower corona, and the radio emission in the decameter range is generated by the upper corona and so on (Zheleznyakov, 1970). An important component of solar activity is various types of solar bursts. Solar bursts can serve as a probing signal to study properties of solar corona plasma. Multi-frequency observations of solar radio emission allow ones to determine the electron density, temperature and magnetic field strength in the solar corona at different heights.

In the decameter range the solar activity are observed in the type III bursts associated with IIIb bursts, U and J bursts, the type II and IV bursts, striae, drifting pairs and S-bursts as well as other events (Krüger, 1979). They occur with varying frequency of occurrence. The main parameters characterizing the bursts are the frequency drift rate, instantaneous bandwidth, duration, flux, polarization, etc. All these parameters indicate the type of solar bursts. The type III bursts is the most numerous collection of solar bursts recorded in radio observations. They occur on the whole Sun. However, the most of observations are performed by ground-based instruments, and a significant part of solar radio events is unavailable for the radio astronomy tools. This situation is improved by space mis-

sions such as WIND and STEREO, but they are not as sensitive as the newest radio telescopes LOFAR, UTR-2, GURT and others. Nevertheless, some solar bursts from the far side of the Sun can arrive at ground-based telescopes due to specific conditions in solar corona. Such events are related to solar bursts with high-frequency cutoff. Recall, the low-frequency cutoff (radio emission below 10 MHz cannot reach to ground-based instruments) in cosmic radio emission appears due to the ionosphere. As for the high-frequency cut-off, its cause is totally different. This effect is explained by the burst's source position in solar corona with respect to the observer. Really, if the source is moved radially from behind the solar limb, it may be occulted by solar corona. Therefore, the most high-frequency part of the solar burst spectrum is reflected away from the direction of the Earth. The propagation of radio emission of behind-limb solar bursts in the solar corona imposes a number of features on the characteristics of these bursts for terrestrial observers.

In this work we present preliminary results related to the observations of solar bursts with high-frequency cutoff (Fig.1), demonstrating clearly the properties typical for the type III ones. The identification is useful for understanding their nature and frequency-time evolution.

2. Instruments and observations

On 19 August of 2012 starting with 8:23 UT the Ukrainian decameter radio telescope UTR-2 (8-33 MHz) has registered about a dozen of solar bursts following each other. Their main peculiarity was high-frequency cutoff near to the upper boundary frequency of observations for UTR-2. Note that we used only four sections of the north-south antenna array of this radio telescope. The total effective area of such an antenna part is 50 000 m^2, and the beam pattern size is 1º×15º at 25 MHz. The solar radio data were recorded by the digital DSP spectrometer operating in the frequency range of 9-33 MHz with the time resolution of 100 ms and frequency resolution of 4 kHz. Some of these solar bursts had their cutoff frequency above frequency capabilities of UTR-2. To get a full view of all the events, we have studied the observations of two different radio telescopes at the same time: the French Nançay Decametric Array (10-70 MHz) and the Italian San Vito Solar Observatory of RSTN (25-180 MHz). Both the instruments also show the registration the given bursts. This allowed us to find the frequency of cutoff of each bursts in the collection. They were different from burst to burst and lie in the range of 30-55 MHz. The simultaneous

observations in different parts of the world indicate that the given bursts and their characteristic features have solar origin rather than either ionospheric or instrumental links.

The frequency drift rate of the solar bursts was negative, 1.1-3.3 MHz/s that corresponds to the characteristic values as applied to the type III bursts in decameter wavelengths. The same is related to their duration. The flux of the set does not exceed 1000 s.f.u. (1 s.f.u. = 10^{-22} W m^{-2} Hz^{-1}) that points to the moderate character of bursts in intensity.
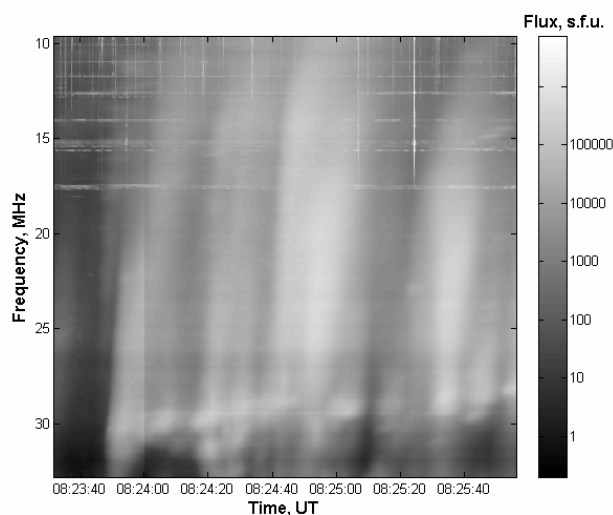

Figure 1: Dynamical spectrum of solar radio bursts with high-frequency cutoff, observed on 19 Augusts of 2012 after 8:23 UT by the telescopes UTR-2. Horizontal bright lines are disturbances due to broadcasting radio stations. Vertical lines in the range about 8-18 MHz indicate terrestrial lightning discharges.

In this connection it should be mentioned that recently a solar burst with high-frequency cutoff in the decameter range of wavelengths has been described by Brazhenko et al. (2012). This was a single radio event on 3 June of 2011. It had the cutoff at ~27.5 MHz, the half-power duration 17-22 s, the frequency drift rate 100-500 kHz/s. Moreover, the dynamical spectrum of this event demonstrates an unusual fine structure with filaments called "caterpillar". The unique properties of this burst make it difficult to classify, according to the conventional scheme of types of solar bursts. Therefore, the further patrol of new events with high-frequency cutoff is very important for a successful interpretation of the phenomena.

3. Interpretation

As it has been shown by Melnik et al. (2012), one of plausible interpretations, explaining features of the unusual burst on 3 June of 2011, is that the origin of the event came from behind the solar limb, and the cutoff of its radio emission appeared because the high-frequency part of the burst's spectrum does not pass towards the Earth. This approach also can be applied for the group of solar bursts observed on 19 August of 2012. Really, the solar activity was connected with a new group of solar spots (AR 11548, about N19E87) born 17 August 2012 on

the far side of the Sun for terrestrial observers. This is supported by the STEREO observations (see http://stereo-ssc.nascom.nasa.gov/data.shtml). However, the plasma dispersion of solar corona influences on the direction of radio wave propagation that can lead to the reflection of radio rays away from the Earth rather than their refraction towards the Earth (see, for example, Thejappa and Mac-Dowall, 2010). Consequently, the purely spherical model of solar corona density is not favorable for behind-limb solar bursts to detect them by ground-based tools. The situation may be rescued by coronal mass ejections (CMEs) associated with the post-limb flare activity. In particular, the CMEs generate lower-density cavities in solar corona (Gibson S.E. et al., 2010) through which the radio emission of behind-limb bursts can fall to Earth. This problem will be considered in more detail elsewhere.

4. Conclusions and future work

In this work we have shown that the solar bursts with high-frequency cutoff can be identified as usual type III bursts. Because of various effects of radio wave propagation in solar corona (generally speaking, the latter is an inhomogeneous medium), being originally the type III bursts, the behind-limb bursts are distorted. Maybe that is why the bursts on 3 June of 2011 looks like "caterpillar". Anyway, the analysis of ray tracing in inhomogeneous solar corona for the solar bursts with cutoff requires a separate examination. Additionally, notice that it would be useful to check the functional evolution of frequency drift rates and durations in frequency for the events on 19 Augusts of 2012 considered in this paper. According to Alvarez and Haddock (1973), as well as Elgarøy and Lyngstad (1972), there are characteristic dependences of the frequency drift rate and the duration in frequency, supported by ordinary type III bursts. It would be useful to check them as applied to the bursts of this paper in future.

References

Alvarez H., Haddock F.T.: 1973, *Sol. Phys.*, **29**, 197.
Brazhenko A.I. et al.: 2012, *RPRA*, **3**, 279.
Elgarøy Ø., Lyngstad E.: 1972, *A&A*, **16**, 1.
Gibson S.E. et al.: 2010, *ApJ*, **724**, 1133.
Krüger A.: 1979, *Introduction to Solar Radio Astronomy and Radio Physics*, Springer, Berlin.
Melnik V.N. et al.: 2012, *RPRA*, **17**, 199 (in Russian).
Thejappa G., MacDowall R.J.: 2010, *ApJ*, **720**, 1395.
Zheleznyakov V.V.: 1970, *Radio Emission of the Sun and Planets*, Pergamon Press, Oxford.

ON THE E/P-COSMIC RAYS AS MEDIATORS OF VISCOUS FORCES THAT CREATE SHOCK AND VORTEX STRUCTURES IN THE RADIO GALAXIES

N.O.Tsvyk

Institute of Radio Astronomy of NAS of Ukraine,
Chervonopraporna 4, 61002, Kharkiv, Ukraine, *natalitsv69@gmail.com*

ABSTRACT. There are for the galaxies of FRII type (like Cygnus A) studied a number of hydrodynamic and kinetic processes to transport of magnetized plasma with cosmic rays, and a stratification process of RG-lobe because of e\p-cosmic rays. We found that the jet and bow shock in radio galaxies are supported by the processes of e\p-cosmic rays (acceleration, radiation), and the effects of changes in viscosity inside the cocoon. Cosmic rays are working inside the "jet head" into the cocoon stratification: to the light caviton (with high kinematic viscosity) and to the heavy shock cover (with high magnetic viscosity). The post-jet-vortex is injected by diffusion of e-rays through the area of "jet head" MHD-turbulized, and it is flowing a caviton around. Alternatively, the bow shock accompanied super sound turbulent waves and flows with p-rays.

Keywords: Radio galaxy: cosmic rays, viscosity, shocks

1. Introduction. A history for the simulation of the FRII-type radio galaxy lobes

There was in Kaiser (1997) shown a self-consistent hydrodynamical model for the jet-cocoon of FRII radio galaxy (RG), with reconfinement jet-shock (that connected with e-jet plasma production). The other main work, Zanni (2003), show a simple of self-consistent cocoon shock model of FRII RG; and in a work of Kino (2004) was illustrated a hot spot of two-shocks dynamic in details (the parameters of Cygnus A galaxy found).

There are Mathews (2011, 2012) recently shown a model for self-consistent evolution of gas and cosmic rays (CRs) in Cygnus A, in assuming a wind-injection of the viscous e-gas with e-CRs into the lobe (cocoon) of Radio Galaxy. This model shows the post-jet-wind with e-CRs; how e-CRs mix with cluster gas; how viscosity supports the e-wind-flow.

In work of Tsvyk (2010) was discussed a model of RG with two-layer cocoon that separated by e- and p-CRs; and this model is developed here. New points in this report: p-CRs are the shock-inductors; effects of CRs in turbulence and current production; effect of viscosity changes as flow-regulator. We grounded in main assumptions of Mathews (2012), but show the cocoon dynamics in consist with two simple physical structures: a shock-like-outer-layer and a vortex-flow winding the inner-layer. The aim of this work is to study when the main structures of FRII-

RG (jet, cavity-lobes and bow-shocks) are grown up because of stratification effects in the magnetized plasma through the e\p cosmic rays as mediators.

2. The main impacts of the CRs to the FRII-lobe

There key assumptions are: (1) a cocoon matter composed of electron-positron e-plasma (density of $n_e = n_{e1} + n_{e2}$), and ion-proton plasma ($n_p \approx n_{th}$), atoms and neutrals (n_a), e- and p-CRs; (2) a cocoon matter is quasi-neutral ($n_{e1} - n_{e2} = n_{th}$) but current exists in it; (3) the CRs, that have being accelerated by DSA-mechanism near HS and bow shock, are the main mediator of exchanges due to they relativistic properties; (4) the e- and p-CRs separate in different aria because of flow dynamics and viscosity changes; (5) a magnetic field (B) is produced by regular part from the CR-diffusion currents, and by dynamical part (the jet elongated) from pumping in the frozen of e-flows and from the p-CR kinetic effects of mixed matters (mainly within the shock areas). Out the scope are the ions-CRs decays, e-annihilation and many other processes.

The main part of cocoon energy contains in p-CRs; and some essential part is in e-CRs too. The less part cocoon energy contains in B-field, but frozen effects do B-field rule the flow cocoon dynamics. Cocoon energy contains in the p-CRs, the e-CRs, the turbulence (waves and vortexes), the thermal matter and the magnetic field. A jet consists of the e-plasma, with some part of p-plasma; but the p-flows are the most inert and energetically. The e-plasma flows are much frozen in B-fields and they fill the inner-cocoon; against to the p-plasma fills the outer cocoon and pumping shocks because of there momentum. Cocoon stratifies because of viscosity changes and injection of Hill's vortex flows (jet-supported). The radiation of e-CRs (synchrotron in radio, IC in X-ray band) helps for e-plasma vortex glues together and separated from p-plasma turbulence flows.

The jet and the lobes parameters of RG are differ in the shock-like (Zanni, 2003) or wind-like (Mathews, 2011) models. For example, RG of Cygnus A located in cluster of $3 \cdot 10^{14}$ sun-mass and with Virial radius of 1Mpc. The jet length is 60 kpc, bow-shock velocity is ~6000 km/s (0.02c), and the age of this source is ~10 Myr (it adjusts with the observations of e-CRs radio-age, see Machalski (2007)). So, the shock-like model (Zanni, 2003) predicts the RG jet-power of $L_j \sim 10^{47}$ erg/s and the energy of $E_c = 3 \cdot$

10^{61} erg; against to the wind-model Mathews (2012) that give us $L_j \sim 10^{46}$ erg/s and $E_c = 3 \cdot 10^{60}$ erg, that predicts only 1/20 part of cocoon volume fills with e-CRs without p-CRs energy in this wind-model. We review later shock-like model (illustrated in fig.1), and consider that p-CRs energy is essentially.

Bow shock properties in the outer lobe area. Shock-presser equals to the presser of p-CRs in outer lobe, both and nearly equal to the e-CRs presser in the inner lobe (see fig.1: 2, 3-arias, respectively). Pressure of *B*-field is negligible. The number of p-CRs in the outer lobe is some part of p-plasma ($\sim$1-10%); and it is comparable to the number of e-CRs in this area.

Shock dynamic was shown in Zanni (2003). This a shock scale $R_s(t,\theta)$ grows with velocity u_{sh} that defines from the shock presser and the ICM-plasma density, $u_{sh} = dR_s(t,\theta)/dt \sim [P(t)/\rho_1(t)]^{1/2}(\cos^2\theta + a_1)$, and has an elongation along the jet-direction (for $\theta=0$ we have $1+a_1 \sim 1.3$). The other way, the energy of cocoon defines from the jet burst power (that comes with flow injection of e-CRs plasma), and as well as from shock presser multiplied to cocoon volume, $E_c(t) \sim \int L_j(t)dt \sim P(t) R_s(t,0)^3$. The jet plasma is strongly blown to the inner lobe (3-area in fig.1), and it compresses the cluster matter of outer lobe (1-area, ICM) into the bow-shock front (2-area).

The flow velocities are super-sonic and not regular behind the shock front. Here is the turbulence dominated in plasma dynamics that pumps the Meshkov-vortex instabilities and ejects the inner-lobe-flow vortex surrounding bow-front. The e/p-CRs help to transport shock energy because there high transcalency. The jet-hot-spot, being the shock-center-point, forms the caviton-like feature in density map (see fig.1: 3, 4-arias) which may work to focus the wave-shock energy and support the jet.
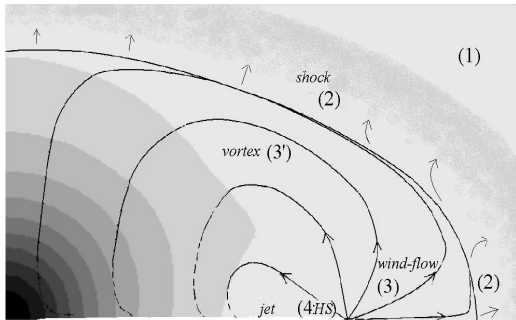

Figure 1: The density field (gray scales) and the velocity field (vector-lines) within the inner (3) and outer lobes (2).

Wind-flow properties in the inner lobe-caviton area. Wind-flow dynamic was shows in Mathews (2011, 2014); the simplest model is "simple-source" injection of e-flux-matter with e-CRs into the outer-lobe ep-plasma (with some part of neutral atoms). It illustrated in fig. 1 see aria 3; and the model of parameters done in Tables 1, 2. The pressure (*P*) and flow velocity (*u*) make the dynamical variations such as in the injection point (hot spot at jet-head) we have $P \rightarrow 0$ and *u*-velocity is maximum. The average flow velocity consists with regular and diffusion parts, the density varies with velocity profile, as $\rho \propto r_s^{q-2}$ when $u \propto (c/3)r_s^{-q}$, ($q \leq 2$, r_s is a scale from HS to

the chosen point). It is likely that post-jet e-plasma wind to the lobe (3) as nearly regular flow together with e-CRs and some part of thermal plasma from area (2), because this matters have mixed gradually within the HS-area and accompanied the accelerations of the e-CRs. That way, in the injection HS-point we have a purely post-jet flow with the density as in Kino (2004) model (see Table 1); and then the post-jet flows mix with $\sim 0.2n_{th}(r)$ of outer thermal plasma because of e-CR diffusion (see Table 2; *r* is a scale from RG-center to the chosen point, a density derives in the King's model as $n_{th}(r) \propto (1+r^2/a_K^2)^{-1.13}$). This e-dominated-flow becomes regular because of viscosity in wind-injection area. Latter, in outside, the flux-collision-front give us the maximum of presser, that exhibit as *u*=0 and thermal-heats dominate. In this flow-stress cover, where the wind-flow transforms into the macro-scale Hill's-2 vortex, we have: $\rho_e u \sim \rho_{th}u_2$, $u_2 \approx 0.75\ u_{sh}$; and the matters are mixed strongly by vortex-turbulence and MHD-waves, as e-CRs pressure is comparable to thermal pressure, $P_{th} \geq P_{eCR}$. So, the wind-velocities and Hill's vortex velocity are correlated here.

Table 1: The parameters of Cygnus A at near HS-area based on Kino (2004) model: the density (ρ and n_a, n_p, n_e), magnetic field (*B*), scattering time (τ), viscosities (η_K, v_K, v_m), collision (X=$\omega_B\tau$; $\beta \sim 0.3$) and Reynolds (*Re*) numbers.

	1-ICM	2-HS	3-HS	4-jet
Presser, dyne/cm^2	10^{-10}	$2\ 10^{-8}$		$<10^{-8}$
n_a/n_p	0.20	0.05	<0.01	0
n_p;cm^{-3},	0.025	0.1	10^{-5}	10^{-7}
n_e, cm^{-3}	0.025	0.1	10^{-3}	10^{-4}
B, G	10^{-5}	$7 \cdot 10^{-5}$	$2 \cdot 10^{-4}$	$2 \cdot 10^{-5}$
ρ, m_p/cm^3	0.03	0.1	10^{-5}	$6 \cdot 10^{-7}$
$\omega_B\tau_{ii}$, $[\omega_{Be}\tau_{ee}]$	10^{11}	$[10^{14}]$	$[10^{20}]$	$[10^{19}]$
τ_{ei}, $[\tau_{ee}]$, yr	10^5	10^7	$[10^{12}]$	$[10^{12}]$
η_K, gm/(s cm) *(β=0.3)*	$5 \cdot 10^{-5}$	0.25	35	10
v_K, *(β=0..0.3)*	$10^{\ 25..21}$	$10^{29..24}$	$10^{37..30}$	$10^{36..31}$
v_m, cm^2/s	$10^{\ 21}$	10^{20}	10^{14}	10^6
Re=$\lambda_0 c/v_K$ *(β=0.3, $\lambda_0 \sim$1kpc)*	$10^{\ 11}$	$5 \cdot 10^7$	50	10

Vortex properties in the inner lobe-caviton area. Some of the vortex-flow dynamic with vortex-injection was shows in Antonuccio-Delogu (2010). We add this sketch of processes some more connection with shock-structures. This way, the main vortex is injected by Carioles force in around of min-pressure-focus ($P \rightarrow 0$) that forms as a ring near the hot spot points because of flux-stress dynamic in the post-jet structures of e-flux-matter blows. The injection provides within Kelvin's low frames: $d(\vec{\omega}/\rho)/dt = (\vec{\omega}/\rho)\nabla\vec{u}$ (ω-circulation is constant, $\vec{\omega} = rot\ \vec{u}$). And the gravity-buoyant and F_η-viscosity forces help us to form the vortex flux of Hill's-2 like type

in the post-jet cavity surface around (see fig.1, 3' area), because of the matter difference and e-CR presser variation:

$$\frac{\partial \vec{u}}{\partial t} + \rho^{-1}\nabla P + \tfrac{1}{2}\nabla(u^2) = [\vec{u} \times \vec{\omega}] + \vec{F}_\eta + \vec{F}_g \cdot$$

A simple model of Hill's-2 vortex of R_{s3} size (limited of e-plasma contact border, $R_{s3} \sim 0.7\,R_s$) may describe as main-flow-vortex in nearly uncompressed matter by the velocity profile in spherical (r-θ) geometry with the RG centre as zero-point and jet aligns to θ=0:

$$u_r \propto \rho_{th}(r)^{-1}\,(R_{s3}(t,\theta)^2 - r^2)cos\theta\,cos(2\theta);$$
$$u_\theta \propto \rho_{th}(r)^{-1}\,(R_{s3}(t,\theta)^2 - r^2)cos\theta\,sin(2\theta).$$

A fine density variation is accounted as $u \propto \rho_{th}(r)^{-1}$ in attached to the King's model. This main-vortex excites the vortex-turbulence in contact with shock-surface that runs plasma density to mix by everyone small or large flow-velocity lines. The turbulence makes to shift dynamically this Hill's vortex forward together with bow-shock surface. The plasma presser inside the any macroscopic flow tube is decrease because the e-CRs are radiated, and this supports the Carioles force in Hill's-2 vortex structure.

Vortex flux matter composed with e-plasma and e-CRs that predominates over the thermal ep-plasma in the inner cocoon part ($n_e > n_{th}$). This forms a cavity-vortex structure within the inner e-Lobe density field, $\rho = (n_{th} + n_a)m_p + n_e m_e$, and the Hill-2 vortex injection helps to separate the inner-matters with e-CRs from outer-matters with p-CRs. The particles are sorted by quasi-neutrality low ($n_{e1} - n_{e2} = n_{th}$).

The average flux velocity (u) obtains as to dominate the e-plasma flux and the relativistic e-CR diffusion flux: $u = (\Sigma\,n_\alpha\,m_\alpha\,u_\alpha)/\rho$ (α is types of particles: ($e1$, $e2$) – electron/ positrons, p – protons, a – neutral atoms, and $e\backslash p$-CR – relativistic particles). Superposition of the vortex and the shock velocity gives up the flux relaxation ($u \to 0$) at $\theta \sim \pi/2$. Near the e-lobe edge (R_{s3}-surface) we have $u \sim u_2$; and in this area the matter composition changes: the e-plasma is depressed and the thermal plasma with p-CRs is added, whit the presser is conserved.

To construct the density model (fig. 1, Table 2) we use the continuity matter equation with referred assumptions and with u-flux model chosen.

3. Magnetic fields impact to FRII-lobe structure

The magnetic field is grown both the dynamical and regular field parts inside the cocoon. The dynamical field is pumping from cosmic turbulence B_{turb} field by adiabatic and alpha-pump turbulent effects; the regular part of B_0-field induced from CR-diffusion currents.

Only estimation lobe model parameters are represented in Table 2, and the B-field calculations in this model show in fig.2. If the current is estimated in the inner lobe because of diffusion motion of the e-CR-particles with the different singles, $\Delta n_e \sim \Delta n_{CR} \sim 0.1\,n_{th}$ (despite of $n_e >> n_{th}$ in the 3-area) and $\Delta v \sim |v_e - u| \sim <v_{dif}> \sim 10^6$ cm/s (that is smaller then sound and Alfvenic velocities, $c_{s,A} \sim 10^7..10^9$ cm/s), so the regular part of magnetic field give us tor-

oidal-field of $B_0 \sim 3 \cdot 10^{-4}$ G that mainly induced by radial and jet-elongate current components.

Beside this, the p-CRs diffusion give us a moves B-field lines together with cosmic matter, and pumps dynamically the turbulent field component as alpha-pump turbulent effects in (2) and HS areas (fig.1). These effects are dominated within the outer lobe that is near the bow shock-wave surface; we assume that $B_{turb} \propto (P_{eCR} + P_{pCR})$. Stress of these turbulent fields must be $B_{turb} \sim 3 \cdot 10^{-4}$ G, compare to the regular B_0-field near the jet-HS surface.

Maximum strength of regular magnetic field (B_0) is nearly denoted to the areas of minimum plasma presser (the same as areas of with minimum of Hill's-flow velocities). This effect comes to gluing of local e-flows with e-CRs, and it may appear as bright features (look likes as an additional HS-spot) in radio emission map of the RG-lobe. However the turbulent pumping may be so strong that to exhibit only one HS-point in the lobe map as the jet head.

Table 2: The model parameters of inner and outer lobe for typical FRII-RG (like Cygnus A) based on assumption of the wind-vortex-shock cocoon transformation because of the CR-flow dynamics (see the text and Table 1 in detail).

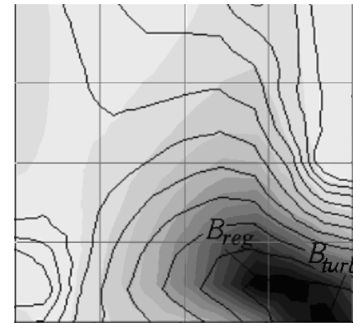| AREA	3 (HS)	2 (HS)	3 (e-Lobe)	2 (outer)
n_e	0.001	0.0005	10^{-4}	$<10^{-4}$
n_{th}, cm^{-3}	0.001	0.04	0.002	0.003
n_a	10^{-6}	0.0003	$<10^{-4}$	$<10^{-4}$
B_0, mG	0.15..0.2	0.03	0.3…0.2	0.06
Λ_{ll} ..	0.1 ..	0.1 ..	0.5 ..	10 ..
Λ_r, kpc	10^{-5}	10^{-6}	0.1	0.5
ν_m	10^{13}	10^{15}	10^{18}	10^{19}
ν_K*	10^{35}	10^{31}	10^{13}	10^{20}
$Re = \lambda_0 c / \nu_K$*	<1 *(reg. flow)*	~ 2	$10^7..10^{20}$ *(turb.)*	$\sim 10^{13}$
λ_{min}, pc ($Re \sim 1000$)	$>10\,000$	>1	$<10^{-6}$	<0.1
* parameters at magnetic line intermittency β=0.3;				
Λ is min CR-diff. length; λ_{min} is min vortex scale at $Re \sim 1000$				

Figure 2: The model of magnetic field strength (in the gray scales: dark is $B \sim 3 \cdot 10^{-4}$ G, white is $B \sim 10^{-6}$ G) and the low-band synchrotron radiation (contour lines).

4. Model for the RG lobe viscosity as cosmic plasma

Cosmic plasma is low-collision matter (the collision term is $X_\alpha = \omega_{B\alpha}\tau_\alpha \gg 1$, and the magnetic presser is smaller then thermal one $P_B < P_{nT}$), and this plasma is composed of the different types (α) of particles, that parameters are changed within the RG-cocoon.

The contact layer that splitting the inner lobe (3) with e-plasma and the outer lobe (2) with thermal plasma plus p-CRs, is the front of viscosity stress that comes to change the matters dynamics. Viscosity consists of kinematical and magnetic parts, and the physics of cocoon are coordinated by these types of viscous vary.

This way, the kinematical viscosity η_K coordinates the changes of the velocity along B_0 (by η_{K1}), and the viscous dump of transverse velocity fluctuations (by $\eta_K \sim \eta_{K0}$). Here we are: $\eta_{K1} \sim \eta_{K0} X_j^{-2+\beta}$, where $\eta_{K0} = \Sigma\{n_j T_j \tau_j X_j^{-\beta}\}$ and $0 < \beta < 1$ is the magnetic turbulence parameter. The p-CRs make to change the characteristics X and β of the slow matter turbulence that handle the viscous forces.

The magnetic viscosity, $\eta_m = \rho \nu_m = \rho\, c^2/\sigma_{eff}$ coordinates the currents induction and the enhanced of MHD-turbulence within the shock both and in the jet surface; both and it enhanced the magnetic dynamo in the dense matter area. Here is the effective conductivity within e-lobe depends on the neutral density $\sigma_{eff} \sim e^2 n_e \tau_e\, m_e^{-1}(1+ (n_a m_p \rho^{-1})^2 X_e X_i)$ as accounted in Bykov (2007) model.

Table 1 and 2 demonstrate the typical parameters in cocoon as changes of the kinematical and the magnetic viscosity, both and as turbulent exiting changes (by Reynolds number). The fig.3 demonstrates the relative viscosity changes of ν_m/ν_K that response the areas where magnetic turbulence may pump strongly.
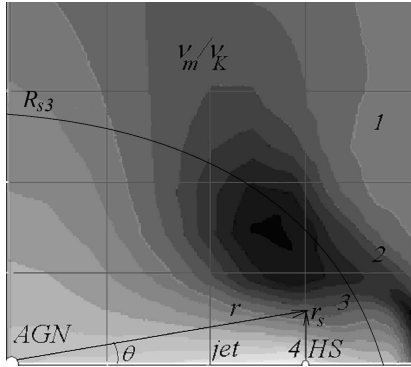

Figure 3: The model of relative viscosity changes (in the gray scales: dark is $\nu_m/\nu_K \sim 10^{10}$, white is $\nu_m/\nu_K \sim 10^{-20}$; the 2-3 contact R_{s3}-boundary outline schematically sketched).

5. Radiation and streaming of the e-CRs in FRII lobe

In the inner lobe, the wind-flow consists of the local flows with e-CRs which are gluing because of viscosity, magnetize effects and radiating cooling of e-CRs. The diffusion effect of the e-CRs, because of vortex and Alfven-wave turbulence, are smoothing the flow dynamic and dumping turbulence by viscosity driven. The effect of e-CRs radiation leads to cool of the lobe matter and it helps a current production and gluing of local e-CR-flows.

The e-CRs are radiating mainly by synchrotron (in radio bands at f-frequency) and synchrotron-inverse Compton (in X-ray bands) processes, which are frequency-dependent. So, the lobe radio brightness is $I_{syn} \propto n_{eCR}\, B\, f^{(-s+1)/2}$, and the X-ray brightness depends on n_{eCR} and radiation field.

The e\p-CRs flow together with the thermal plasma (that frozen in B-field tubes) and drift with energy-dependent diffusing velocity, $v_{eCR} = u + v_{diff\_eCR}$. A diffusion velocity defines by turbulence parameters and regular magnetic field (B_0): $v_{diff\_eCR} \sim (\kappa_{e0}/\Lambda_{diff})\, \gamma^{2-s} \propto (B_0/B_{turb})^2\, r_g\, c/\Lambda_{syn}$. Thus, the low-energy particles of e-CRs, that was cooling by radiation to energy $\gamma \sim 1..10$, have to flow with thermal plasma better then diffuse. Alternatively, the p-CRs particles have to correct a local B_{turb}-lines with any diffusion act, thus in a bow shock area this effects are limited the magnetic field correlation scales (λ_0) with the p-CRs energy spectrum (γ_{p_max}) and with $R_s(t)$ lobe-size.

This way, taking account the trends of B-field and e-flows, we may predicted that a powerful radio emission of low-energy e-CRs in MHz-band comes from areas where e-rays are pulled together into streams, due to the turbulence by viscous forces dumping, and e-rays cooling. And the radiation-cooling of e-CRs give us the main mediator-effects that coordinate all cocoon dynamics.

6. Conclusions

1. The viscosity of RG matter rules in the lobe-phenomenology. It is switching the instabilities, and directing the gluing flows, and heating or accelerating of CRs in the cocoon, and the magnetic-viscosity divides the vortexes into small modes (B-pumping).

2. The bow-shock transports by wave-turbulence, and by the p-CRs, that getting up of magnetic-viscosity the biggest. The e\p-CRs ejects by diffusion-shock acceleration mechanism.

3. The magnetic field turbulence prevents the mixing of cocoon fluid. The e-CRs frozen into magnetic turbulence critically, beginning with $>10^{-6}$ pc-size modes (the smallest). The p-CRs help to mix the matters.

4. The e-CRs and p-CRs are separated by injection of Hill's-2 vortex from relativistic post-jet e-plasma-flow winding. The ties of e-CRs are gluing by viscosity and radiate-cooling effects.

5. The e-CRs diffuse (in adding to flow-transport) by energy-dependent, because of B-turbulence that has been generated by vortexes and MHD-waves.

After synchrotron-radiate-cooling, the low-energy e-CRs are filling nearly all cocoon-volume, adding to the p-CRs that holding up the B-turbulence within the cocoon-surface.

References

Kaiser C.R. et al.: 1997, *MNRAS*, **286**, 215.
Zanni C. et al.: 2003, *A&A*, **402**, 949.
Kino M. et al.: 2004, *MNRAS*, **349**, 336.
Mathews W.G. et al.: 2011, *ApJ*, **736**, 6.
Mathews W.G. et al.: 2012, *ApJ*, **755**, 13.
Tsvyk N.: 2010, in: *Proc. of 10th Gamow's Odessa Astron. Conf.*, Odessa, Ukraine, 142.
Machalski J. et al.: 2007, *A&A*, **462**, 43.
Antonuccio-Delogu V. et al.: 2010, *MNRAS*, **405,** 1303.
Bykov A.M. et al.: 2007, *Physics–Uspekhi*, **50**, 141.

DECAMETER PULSARS AND TRANSIENTS SURVEY OF THE NORTHERN SKY. STATUS, FIRST RESULTS, MULTIPARAMETRIC PIPELINE FOR CANDIDATE SELECTION

V.V.Zakharenko[1], I.P.Kravtsov[1], I.Y.Vasylieva[1,2], S.S.Mykhailova[3], O.M.Ulyanov[1],
A.I.Shevtsova[1], A.O.Skoryk[1], P.Zarka[2], O.O.Konovalenko[1]

[1] Institute of Radio Astronomy of the National Academy of Sciences of Ukraine (IRA NASU)
   4, Chervonopraporna St., 61002, Kharkiv, Ukraine, *rian@rian.kharkov.ua*
[2] LESIA, Observatoire de Paris, CNRS, UPMC, Universite Paris Diderot, Meudon, France
[3] V. N. Karazin Kharkiv National University, 4 Svobody Square, 61022, Kharkiv, Ukraine,
info@karazin.ua

ABSTRACT. We present the results of processing first 20% of Northern sky pulsars and transients survey using UTR-2 radio telescope. Data processing is done by an automatic pipeline that detects and outputs a large number of transient candidates (usually dispersed bursts). We have developed a multivariate pipeline for visual inspection of these candidates. By adjustment of input parameters of the pipeline the observer can substantially increase signal-to-noise ratio of detected signals as well as discriminate them from residual low-intensity interference with high significance. About 450 transient signals have passed the examination by the multivariate pipeline. Their distributions on the Galactic latitude and dispersion measure have been derived. The shape of the distributions suggests that these signals might be associated with cosmic sources of radio emission.

Keywords: pulsars, transients, survey, decameter range

1. Introduction

First decameter-wavelength census of known pulsars (Zakharenko et al., 2013) aimed at re-detection and study of nearby pulsar population was highly successful. More than a half of observable pulsars with dispersion measure (DM) < 30 pc cm^{-3} were re-detected, despite the extremely difficult conditions of observations in the decameter range, such as high Galactic background temperature, large scattering time constant of pulsar pulses, enormously high radio frequency interference (RFI) level etc. The major result of that study was confirmation of pulse profile broadening observed for the majority of aforementioned pulsars, compared to their widths at higher observational frequencies. This opened a new parameter space for searching new sources of pulsed radiation in the closest Galactic neighborhood. Pulse profile broadening can make 'unfavourably' oriented pulsars, rotating radio transients (RRATs) and other radio-emitting neutron stars visible at low frequencies. This makes a low-frequency blind pulsar and transient survey of the entire Northern sky both useful and required.

Such a survey was started in 2010 (Zakharenko et al., 2011). One of the first important results was first detection of decameter emission (Vasylieva et al., 2014) of the re-

cently discovered pulsar J0243+6257 (Hessels et al., 2008). The dispersion measure of this pulsar was substantially refined (an error became less than 0.01 pc cm^{-3} instead of previous one near 0.2). It became possible due to the important advantage of the low-frequency range and broad observational band (16.5 - 33 MHz) of the above survey – the precise determination of the dispersion measure. Observations in a broad frequency band allow to distinguish with high confidence between a real signal that had passed through the interstellar medium and local interference. The real signals have a characteristic dependence of pulse arrival time on the frequency ($\propto f^{-2}$), being delayed at lower frequency f_{min} compared to higher frequency f_{max} by

$$dt = 10^{16}/2.410331 \cdot \text{DM} \cdot (f_{min}^{-2} - f_{max}^{-2}) \qquad (1)$$

seconds. The local signals may have a different origin and time-frequency structure, e.g. signals with linear frequency modulation.

Stream processing of a part of survey data revealed many transient 'candidates'. The goal of the present work is to check each 'candidate' by means of the interactive data reduction pipeline, all intermediate results of which can be inspected simultaneously. For instance, raw dynamic spectra (before de-dispersion) show whether signal's time-frequency shape is not $\propto f^{-2}$ (Vasylieva et al., 2014) or has features similar to those described in (Petroff et al., 2015). Presence of signal only in a narrow frequency band is also an indicator of its artificial origin. However, as the signal-to-noise ratio (SNR) of the candidates after integration of the entire frequency band is quite low, generally 6-8 standard deviations (σ), inspection in the fractional sub-bands reduces it further, sometimes equalizing signal with noise. Therefore, additional criteria are required to verify the signals' origins. Subsequent stage of our work is an analysis of distribution of the 'candidates' on the galactic coordinates and dispersion measures (that can be translated to distance). Similarity of these distributions to distributions of known pulsars and RRATs will imply the cosmic origin of the 'candidates'.

2. Data analysis

The blind decameter drift-scan survey (Zakharenko et al., 2011; Vasylieva et al., 2014) should cover a range of declinations (δ) between -10º and 90º. To date, more than 90% of planned sky region is covered, and about 75% of data is automatically pre-processed (i.e. spared from interference, compensated for interstellar dispersion in the range $0 < DM < 30$ pc cm^{-3} with 0.01 pc cm^{-3} step, producing 3000 spectral-integrated time series that form a "DM-Time" plane, see Fig. 1a). After processing of each observation session, the database of candidates is updated with parameters (occurrence time, DM and signal-to-noise ratio) of detected signals if their SNR exceeds 5.5σ.

At the next stage signals with DM < 1 and signals which form regular structures (usually slanted lines) in the "DM-Time" plane are rejected as they are most likely RFI. Taking into account scattering in the interstellar medium that smears pulses of regular pulsars over tens of milliseconds and pulse width itself, we also reject the events that occupy only a single sample (8 ms x 0.01 pc cm^{-3}) in the "DM-Time" plane.

In order to reveal spurious (RFI-induced) candidates, and to maximize the SNR of real candidates, we have developed a multivariate pipeline for candidate selection. A set of adjustable input parameters includes:

- thresholds in RFI mitigation routine (Vasylieva et al., 2013),
- step between adjacent trial DM values (up to 0.002 pc cm^{-3}),
- cutoff frequency of a high-pass filter that reduces effects of ionospheric scintillations.
- cutoff frequency of a low-pass filter that increases an integration time for the pulses
- width of partial frequency sub-bands
- time interval for search of repetitive signals

When optimal, the above settings lead to 2-5-fold increase in SNR which is vital for exploring spectral features of candidates and their shape in the 'DM-Time' plane with a higher contrast.

Fig. 1 shows visual inspection of a 'candidate' that at first glance didn't provide any reason for rejection (a red disk in the panel a). However, after examining the raw data and its de-dispersion using the correct DM value, we found a signal behavior, very different from that described by equation (1). The signal was relatively narrowband (panel b) and had a linear frequency modulation (panel c, top). Its shape in the time-DM plane is smeared over many adjacent DM values (panel c, bottom) as it happens with RFI signals. Signals like in Fig. 1 are of course excluded from 'candidates' database.

3. Results and discussion

As a result, 'candidates' from about 20% of the survey have been checked for compliance with the dispersion law (equation 1). These signals have a relatively broad band and don't show any RFI features. We determined approximate coordinates of each 'candidate' by deriving direction of UTR-2 pointing at the moment of its detection.
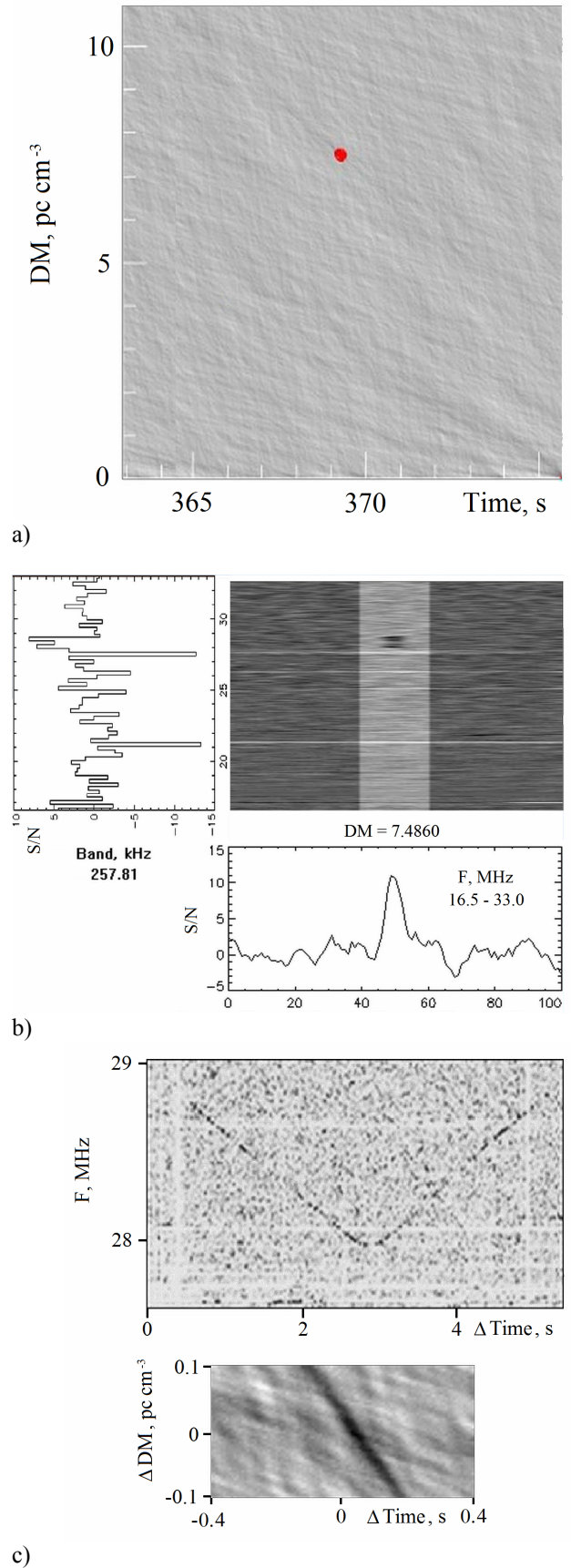

a)

b)

c)

Figure 1: (a) "DM-time" plane, (b) de-dispersed spectrogram (grey-scale image) with cut-sets over time and frequency, (c) zooms of raw spectrogram (top) and "DM-time" plane (bottom)

A map of Galactic background radio emission (Sidorchuk et al., 2008) and superimposed coordinates of the corresponding transient sources are shown in Fig. 2. Only recordings of low declinations are (partly) processed so far.
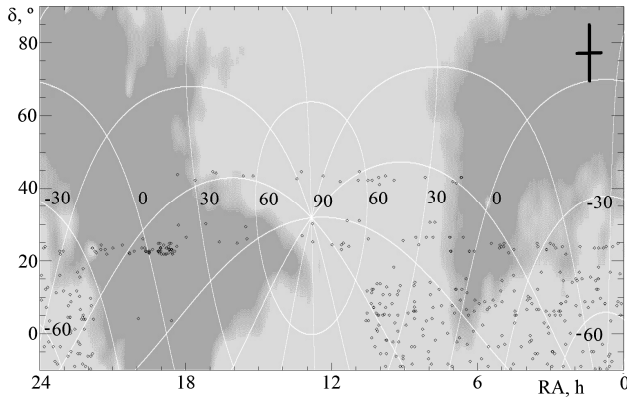

Figure 2: Sky map with coordinates of transient candidates and pattern of directivity of the UTR-2

A promising result is a lack of preferable directions in the distribution of the sources, except for a region of RA=19^h and δ = 23°. But as this region is located close to Galactic disk, in the direction not far from its center, this concentration of detected events seems expected.

To analyze statistically whether the above sources are a part of Galactic disk population, we have derived a histogram of their galactic latitudes. As expected, the histogram has a local maximum near b=0° (Fig. 3 a), similar to the histogram for close pulsars (period > 0.2 s, DM < 30 pc cm^{-3}), shown in Fig. 3b (derived from Manchester et al., 2005).
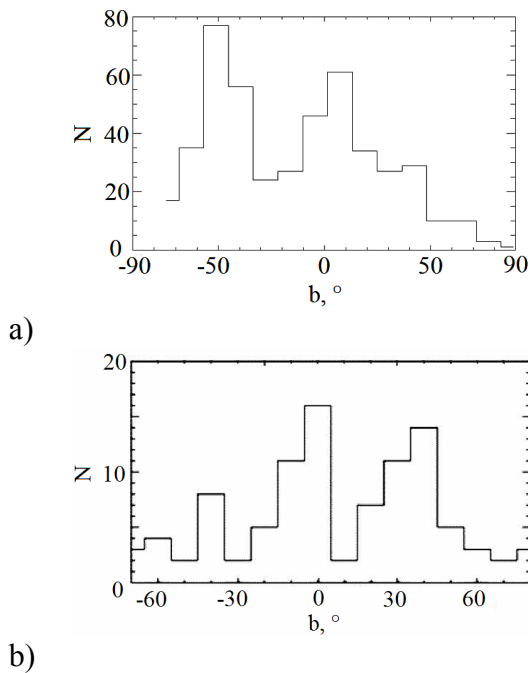

a)

b)

Figure 3: Histogram of transients' (a) and known close pulsars' (b) (Manchester et al., 2005) galactic latitudes

The main maximum of the histogram is at b= −50°. But from Fig. 2 it is evident that the data with galactic latitude from −45° to −90° is processed completely, whereas the remaining areas are processed partly. Therefore, along with further data processing the number of events at galactic latitudes above −45° will increase, while below −45° will remain unchanged. Furthermore it is possible that at low radio telescope beam positions (corresponding to low declinations in Fig. 2 and regions with −90° < b <−45°) the number of residual low-intense broadband RFI in the data is higher.

The distribution on the galactic latitude thus implies that if not all, but the majority of detected signals are of cosmic origin and their coordinates tend to low Galactic latitudes. It is possible that there is a number of interference among the 'candidates', but they do not have a large impact on the shape of the distribution.

The expected distribution of cosmic sources on DM is shaped by the following factors. With increasing DM (and therefore distance between a source and an observer) the geometrical size of the considered region (layer), and therefore the number of sources that it contains, should increase. For the closest ones (while the considered layer doesn't extend beyond the width of the Galactic disk) the number of sources grows approximately as a square of distance (and hence of DM). For more distant sources the increase will be close to linear. However at some point this distribution will reach the maximum and the number of sources will start to decrease, because the more distant sources are generally weaker. Additionally, with decreasing frequency, the scattering of pulsed signals comes into play (the scattering time constant is ∝ f -4). I.e. at lower frequencies this turnover should happen at lower values of DM, compared to higher frequencies.

For comparison, a simulation of similar distributions for pulsars, expected to be detected by SKA1-LOW and SKA1-MID is shown in Fig. 4 (Keane et al., 2015). A distribution, obtained for the above 'candidates' is shown in Fig. 5a, and is generally in agreement with the simulated one (Fig. 4), as we see the increase in number of 'candidates' up to DM=10-15, followed by a gradual decrease.
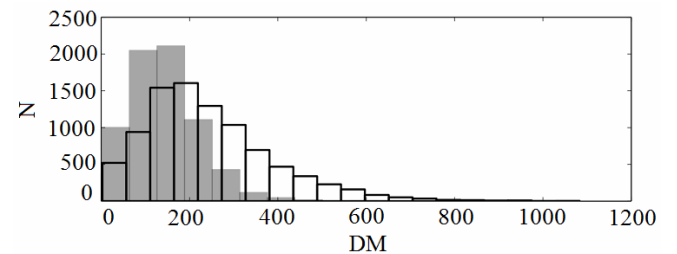

Figure 4: Simulated histograms of DM of pulsars, expected to be observed with SKA Phase 1, for SKA1-LOW (dark bars) and SKA1-MID (clear bars) (Keane et al., 2015)

Apart from an outlier at a low DM value (that can be related either to RFI or to unidentified source of repetitive pulsed emission, e.g. a pulsar) the distribution is smooth. For comparison, Fig. 5b shows a distribution of known

RRATs on dispersion measure, derived from 'RRATalog'. It has a fragmented structure due to a small number of sources, but as a whole, it is also similar to those shown in Fig. 4 and Fig. 5a. We should note that the shape of RRAT distribution is a result of their discoveries in high-frequency surveys – at decimeter wavelengths, which means the lower influence of the interstellar medium and a larger DM range that can be explored.
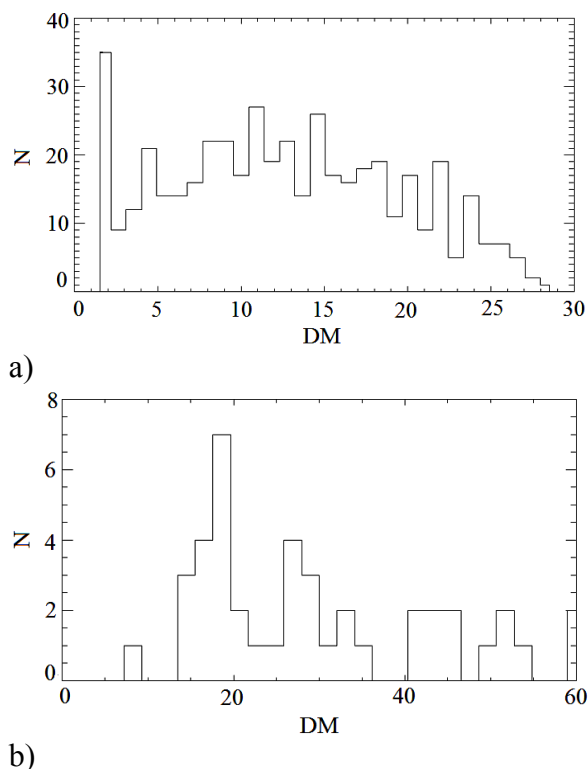

a)

b)

Figure 5: Distribution of DM of transient events detected in this study (a) and known RRATs (b) (RRATalog)

Thus, the both distributions that we derived (on the galactic latitude and DM) suggest that the majority of detected signals are most likely of cosmic origin. The shape of the received pulses is similar to pulsar or RRAT pulses. We assume that the detected 'candidates' could originate from:
• neutron stars that are unfavorably oriented in space for higher frequency observations,
• RRATs with low dispersion measures that have been misinterpreted as RFI in the high-frequency surveys,
• pulsars that present an increase of flux density towards low frequencies (such as PSR B0943+10, see Stappers et al., 2011),
• giant pulses of millisecond pulsars (usually flux density of millisecond pulsars grows with decreasing frequency) that are either sporadic or unfavorably oriented. Although giant pulses are short, they will arrive significantly scattered at our frequencies and will be noticeable in the survey data,
• anomalously intense pulses (see Ulyanov et al, 2006) of close weak pulsars.

4. Conclusions

Using the developed routines of multivariate candidate selection, we have analyzed the transient signals from about 20% of the decameter pulsars and transients survey of northern sky. Adjustment of filtering parameters and simultaneous access to all intermediate stages of processing serves for rejection of RFI-induced candidates even with low SNR.

Histograms of candidates' galactic latitudes and dispersion measures show that corresponding sources tend to be located at low Galactic latitudes and have an expected distribution on dispersion measure. This allows us to suppose that the majority of above signals must be associated with cosmic sources.

Complete processing of all survey data give more significance to these distributions and possibly will allow to link such parameters as galactic longitude, intensity, probability of occurrence etc. This will help to attribute the sources to certain structures, such as Gould belt, Galactic spiral arms and subsequently to improve general knowledge of close neutron star population.

References

Zakharenko V.V. et al.: 2013, *MNRAS*, **431**, 3624.
Zakharenko V.V. et al.: 2011, *Odessa Astron. Publ.*, **24**, 117.
Vasylieva I.Y. et al.: 2014, *RP&RA*, **19**, 197.
Hessels J.W.T. et al.: 2008, *AIP Conf. Ser.*, **983**, 613.
Petroff E. et al.: 2015, *MNRAS*, **451**, 3933.
Vasylieva I.Y. et al.: 2013, *Odessa Astron. Publ.*, **26**, 159.
Sidorchuk M.A. et al.: 2008, *Astrophysics with E-LOFAR*, http://www.hs.unihamburg.de/DE/Ins/Lofar/lofar_work shop/poster_abstracts.html.
Manchester R.N. et al.: 2005, *AJ*, **129**, 1993.
RRATalog: http://astro.phys.wvu.edu/rratalog
Keane E. et al.: 2015, *AASKA14*, **1**, 40.
Stappers B.W. et al.: 2011, *A&A*, **530**, A80.
Ulyanov O.M. et al., 2006, *IAU Joint Discussion*, **2**, 12.